PHYSICAL REVIEW C **110**, 014905 (2024)

Estimate of background baseline and upper limit on the chiral magnetic effect in isobar collisions at $\sqrt{s_{NN}} = 200$ GeV at the BNL Relativistic Heavy Ion Collider

M. I. Abdulhamid,[4] B. E. Aboona,[56] J. Adam,[16] J. R. Adams,[41] G. Agakishiev,[31] I. Aggarwal,[42] M. M. Aggarwal,[42] Z. Ahammed,[62] A. Aitbaev,[31] I. Alekseev,[2,38] E. Alpatov,[38] A. Aparin,[31] S. Aslam,[27] J. Atchison,[1] G. S. Averichev,[31] V. Bairathi,[54] J. G. Ball Cap,[23] K. Barish,[11] P. Bhagat,[30] A. Bhasin,[30] S. Bhatta,[53] S. R. Bhosale,[18] I. G. Bordyuzhin,[2] J. D. Brandenburg,[41] A. V. Brandin,[38] C. Broodo,[23] X. Z. Cai,[51] H. Caines,[65] M. Calderón de la Barca Sánchez,[9] D. Cebra,[9] J. Ceska,[16] I. Chakaberia,[34] B. K. Chan,[10] Z. Chang,[28] A. Chatterjee,[17] D. Chen,[11] J. Chen,[50] J. H. Chen,[20] Z. Chen,[50] J. Cheng,[58] Y. Cheng,[10] S. Choudhury,[20] W. Christie,[6] X. Chu,[6] H. J. Crawford,[8] G. Dale-Gau,[13] A. Das,[16] T. G. Dedovich,[31] I. M. Deppner,[22] A. A. Derevschikov,[43] A. Dhamija,[42] P. Dixit,[25] X. Dong,[34] J. L. Drachenberg,[1] E. Duckworth,[32] J. C. Dunlop,[6] J. Engelage,[8] G. Eppley,[45] S. Esumi,[59] O. Evdokimov,[13] O. Eyser,[6] R. Fatemi,[33] S. Fazio,[7] C. J. Feng,[40] Y. Feng,[44] E. Finch,[52] Y. Fisyak,[6] F. A. Flor,[65] C. Fu,[29] T. Gao,[50] F. Geurts,[45] N. Ghimire,[55] A. Gibson,[61] K. Gopal,[26] X. Gou,[50] D. Grosnick,[61] A. Gupta,[30] A. Hamed,[4] Y. Han,[45] M. D. Harasty,[9] J. W. Harris,[65] H. Harrison-Smith,[33] W. He,[20] X. H. He,[29] Y. He,[50] C. Hu,[60] Q. Hu,[29] Y. Hu,[34] H. Huang,[40] H. Z. Huang,[10] S. L. Huang,[53] T. Huang,[13] X. Huang,[58] Y. Huang,[58] Y. Huang,[12] T. J. Humanic,[41] M. Isshiki,[59] W. W. Jacobs,[28] A. Jalotra,[30] C. Jena,[26] Y. Ji,[34] J. Jia,[6,53] C. Jin,[45] X. Ju,[47] E. G. Judd,[8] S. Kabana,[54] D. Kalinkin,[33] K. Kang,[58] D. Kapukchyan,[11] K. Kauder,[6] D. Keane,[32] A. Kechechyan,[31] A. Khanal,[63] A. Kiselev,[6] A. G. Knospe,[35] H. S. Ko,[34] L. Kochenda,[38] A. A. Korobitsin,[31] A. Yu. Kraeva,[38] P. Kravtsov,[38] L. Kumar,[42] M. C. Labonte,[9] R. Lacey,[53] J. M. Landgraf,[6] A. Lebedev,[6] R. Lednicky,[31] J. H. Lee,[6] Y. H. Leung,[22] N. Lewis,[6] C. Li,[50] D. Li,[47] H-S. Li,[44] H. Li,[64] W. Li,[45] X. Li,[47] Y. Li,[47] Y. Li,[58] Z. Li,[47] X. Liang,[11] Y. Liang,[32] T. Lin,[50] Y. Lin,[21] C. Liu,[29] G. Liu,[48] H. Liu,[12] L. Liu,[12] T. Liu,[65] X. Liu,[41] Y. Liu,[56] Z. Liu,[12] T. Ljubicic,[45] O. Lomicky,[16] R. S. Longacre,[6] E. M. Loyd,[11] T. Lu,[29] J. Luo,[47] X. F. Luo,[12] V. B. Luong,[31] L. Ma,[20] R. Ma,[6] Y. G. Ma,[20] N. Magdy,[53] R. Manikandhan,[23] S. Margetis,[32] H. S. Matis,[34] G. McNamara,[63] O. Mezhanska,[16] K. Mi,[12] N. G. Minaev,[43] B. Mohanty,[39] M. M. Mondal,[39] I. Mooney,[65] D. A. Morozov,[43] A. Mudrokh,[31] M. I. Nagy,[18] A. S. Nain,[42] J. D. Nam,[55] M. Nasim,[25] E. Nedorezov,[31] D. Neff,[10] J. M. Nelson,[8] D. B. Nemes,[65] M. Nie,[50] G. Nigmatkulov,[13] T. Niida,[59] L. V. Nogach,[43] T. Nonaka,[59] G. Odyniec,[34] A. Ogawa,[6] S. Oh,[49] V. A. Okorokov,[38] K. Okubo,[59] B. S. Page,[6] R. Pak,[6] S. Pal,[16] A. Pandav,[34] A. K. Pandey,[29] Y. Panebratsev,[31] T. Pani,[46] P. Parfenov,[38] A. Paul,[11] C. Perkins,[8] B. R. Pokhrel,[55] M. Posik,[55] A. Povarov,[38] T. Protzman,[35] N. K. Pruthi,[42] J. Putschke,[63] Z. Qin,[58] H. Qiu,[29] C. Racz,[11] S. K. Radhakrishnan,[32] A. Rana,[42] R. L. Ray,[57] H. G. Ritter,[34] C. W. Robertson,[44] O. V. Rogachevsky,[31] M. A. Rosales Aguilar,[33] D. Roy,[46] L. Ruan,[6] A. K. Sahoo,[25] N. R. Sahoo,[26] H. Sako,[59] S. Salur,[46] E. Samigullin,[2] S. Sato,[59] B. C. Schaefer,[35] W. B. Schmidke,[6,*] N. Schmitz,[36] J. Seger,[15] R. Seto,[11] P. Seyboth,[36] N. Shah,[27] E. Shahaliev,[31] P. V. Shanmuganathan,[6] T. Shao,[20] M. Sharma,[30] N. Sharma,[25] R. Sharma,[26] S. R. Sharma,[26] A. I. Sheikh,[32] D. Shen,[50] D. Y. Shen,[20] K. Shen,[47] S. S. Shi,[12] Y. Shi,[50] Q. Y. Shou,[20] F. Si,[47] J. Singh,[42] S. Singha,[29] P. Sinha,[26] M. J. Skoby,[5,44] Y. Söhngen,[22] Y. Song,[65] B. Srivastava,[44] T. D. S. Stanislaus,[61] D. J. Stewart,[63] M. Strikhanov,[38] B. Stringfellow,[44] Y. Su,[47] C. Sun,[53] X. Sun,[29] Y. Sun,[47] Y. Sun,[24] B. Surrow,[55] D. N. Svirida,[2] Z. W. Sweger,[9] A. C. Tamis,[65] A. H. Tang,[6] Z. Tang,[47] A. Taranenko,[38] T. Tarnowsky,[37] J. H. Thomas,[34] D. Tlusty,[15] T. Todoroki,[59] M. V. Tokarev,[31] S. Trentalange,[10] P. Tribedy,[6] O. D. Tsai,[10,6] C. Y. Tsang,[32,6] Z. Tu,[6] J. Tyler,[56] T. Ullrich,[6] D. G. Underwood,[3,61] I. Upsal,[47] G. Van Buren,[6] A. N. Vasiliev,[43,38] V. Verkest,[63] F. Videbæk,[6] S. Vokal,[31] S. A. Voloshin,[63] F. Wang,[44] G. Wang,[10] J. S. Wang,[24] J. Wang,[50] K. Wang,[47] X. Wang,[50] Y. Wang,[47] Y. Wang,[12] Y. Wang,[58] Z. Wang,[50] J. C. Webb,[6] P. C. Weidenkaff,[22] G. D. Westfall,[37] H. Wieman,[34] G. Wilks,[13] S. W. Wissink,[28] J. Wu,[12] J. Wu,[29] X. Wu,[10] X. Wu,[47] B. Xi,[20] Z. G. Xiao,[58] G. Xie,[60] W. Xie,[44] H. Xu,[24] N. Xu,[34] Q. H. Xu,[50] Y. Xu,[50] Y. Xu,[12] Z. Xu,[32] Z. Xu,[10] G. Yan,[50] Z. Yan,[53] C. Yang,[50] Q. Yang,[50] S. Yang,[48] Y. Yang,[40] Z. Ye,[45] Z. Ye,[34] L. Yi,[50] K. Yip,[6] Y. Yu,[50] W. Zha,[47] C. Zhang,[20] D. Zhang,[48] J. Zhang,[50] S. Zhang,[14] W. Zhang,[48] X. Zhang,[29] Y. Zhang,[29] Y. Zhang,[47] Y. Zhang,[50] Y. Zhang,[12] Z. J. Zhang,[40] Z. Zhang,[6] Z. Zhang,[13] F. Zhao,[29] J. Zhao,[20] M. Zhao,[6] J. Zhou,[47] S. Zhou,[12] Y. Zhou,[12] X. Zhu,[58] M. Zurek,[3,6] and M. Zyzak[19]

(STAR Collaboration)

[1]*Abilene Christian University, Abilene, Texas 79699*
[2]*Alikhanov Institute for Theoretical and Experimental Physics NRC "Kurchatov Institute", Moscow 117218*
[3]*Argonne National Laboratory, Argonne, Illinois 60439*
[4]*American University in Cairo, New Cairo 11835, Egypt*
[5]*Ball State University, Muncie, Indiana, 47306*
[6]*Brookhaven National Laboratory, Upton, New York 11973*
[7]*University of Calabria & INFN-Cosenza, Rende 87036, Italy*
[8]*University of California, Berkeley, California 94720*
[9]*University of California, Davis, California 95616*
[10]*University of California, Los Angeles, California 90095*

---

[*] Deceased

2469-9985/2024/110(1)/014905(18)

[11]*University of California, Riverside, California 92521*
[12]*Central China Normal University, Wuhan, Hubei 430079*
[13]*University of Illinois at Chicago, Chicago, Illinois 60607*
[14]*Chongqing University, Chongqing, 401331*
[15]*Creighton University, Omaha, Nebraska 68178*
[16]*Czech Technical University in Prague, FNSPE, Prague 115 19, Czech Republic*
[17]*National Institute of Technology Durgapur, Durgapur - 713209, India*
[18]*ELTE Eötvös Loránd University, Budapest, Hungary H-1117*
[19]*Frankfurt Institute for Advanced Studies FIAS, Frankfurt 60438, Germany*
[20]*Fudan University, Shanghai, 200433*
[21]*Guangxi Normal University, Guilin, 541004*
[22]*University of Heidelberg, Heidelberg 69120, Germany*
[23]*University of Houston, Houston, Texas 77204*
[24]*Huzhou University, Huzhou, Zhejiang 313000*
[25]*Indian Institute of Science Education and Research (IISER), Berhampur 760010, India*
[26]*Indian Institute of Science Education and Research (IISER) Tirupati, Tirupati 517507, India*
[27]*Indian Institute Technology, Patna, Bihar 801106, India*
[28]*Indiana University, Bloomington, Indiana 47408*
[29]*Institute of Modern Physics, Chinese Academy of Sciences, Lanzhou, Gansu 730000*
[30]*University of Jammu, Jammu 180001, India*
[31]*Joint Institute for Nuclear Research, Dubna 141 980*
[32]*Kent State University, Kent, Ohio 44242*
[33]*University of Kentucky, Lexington, Kentucky 40506-0055*
[34]*Lawrence Berkeley National Laboratory, Berkeley, California 94720*
[35]*Lehigh University, Bethlehem, Pennsylvania 18015*
[36]*Max-Planck-Institut für Physik, Munich 80805, Germany*
[37]*Michigan State University, East Lansing, Michigan 48824*
[38]*National Research Nuclear University MEPhI, Moscow 115409*
[39]*National Institute of Science Education and Research, HBNI, Jatni 752050, India*
[40]*National Cheng Kung University, Tainan 70101*
[41]*The Ohio State University, Columbus, Ohio 43210*
[42]*Panjab University, Chandigarh 160014, India*
[43]*NRC "Kurchatov Institute", Institute of High Energy Physics, Protvino 142281*
[44]*Purdue University, West Lafayette, Indiana 47907*
[45]*Rice University, Houston, Texas 77251*
[46]*Rutgers University, Piscataway, New Jersey 08854*
[47]*University of Science and Technology of China, Hefei, Anhui 230026*
[48]*South China Normal University, Guangzhou, Guangdong 510631*
[49]*Sejong University, Seoul, 05006, South Korea*
[50]*Shandong University, Qingdao, Shandong 266237*
[51]*Shanghai Institute of Applied Physics, Chinese Academy of Sciences, Shanghai 201800*
[52]*Southern Connecticut State University, New Haven, Connecticut 06515*
[53]*State University of New York, Stony Brook, New York 11794*
[54]*Instituto de Alta Investigación, Universidad de Tarapacá, Arica 1000000, Chile*
[55]*Temple University, Philadelphia, Pennsylvania 19122*
[56]*Texas A&M University, College Station, Texas 77843*
[57]*University of Texas, Austin, Texas 78712*
[58]*Tsinghua University, Beijing 100084*
[59]*University of Tsukuba, Tsukuba, Ibaraki 305-8571, Japan*
[60]*University of Chinese Academy of Sciences, Beijing, 101408*
[61]*Valparaiso University, Valparaiso, Indiana 46383*
[62]*Variable Energy Cyclotron Centre, Kolkata 700064, India*
[63]*Wayne State University, Detroit, Michigan 48201*
[64]*Wuhan University of Science and Technology, Wuhan, Hubei 430065*
[65]*Yale University, New Haven, Connecticut 06520*

(Received 24 October 2023; accepted 25 March 2024; published 9 July 2024)

For the search of the chiral magnetic effect (CME), STAR previously presented the results from isobar collisions ($^{96}_{44}\mathrm{Ru}+^{96}_{44}\mathrm{Ru}$, $^{96}_{40}\mathrm{Zr}+^{96}_{40}\mathrm{Zr}$) obtained through a blind analysis. The ratio of results in Ru + Ru to Zr + Zr collisions for the CME-sensitive charge-dependent azimuthal correlator ($\Delta\gamma$), normalized by elliptic anisotropy (v_2), was observed to be close to but systematically larger than the inverse multiplicity ratio. The background baseline for the isobar ratio, $Y = \frac{(\Delta\gamma/v_2)^{\mathrm{Ru}}}{(\Delta\gamma/v_2)^{\mathrm{Zr}}}$, is naively expected to be $\frac{(1/N)^{\mathrm{Ru}}}{(1/N)^{\mathrm{Zr}}}$; however, genuine two- and three-particle correlations are expected to alter it. We estimate the contributions to Y from those correlations, utilizing both the isobar data and HIJING simulations. After including those contributions, we arrive at a final background baseline for Y, which is consistent with the isobar data. We extract an upper limit for the CME fraction in the $\Delta\gamma$ measurement of approximately 10% at a 95% confidence level on in isobar collisions at $\sqrt{s_{NN}} = 200$ GeV, with an expected 15% difference in their squared magnetic fields.

DOI: 10.1103/PhysRevC.110.014905

I. INTRODUCTION

The quantum chromodynamics (QCD) predicts vacuum fluctuations, rendering nonzero topological charges in a local domain with odd $\mathcal{P}$ and $\mathcal{CP}$ symmetries [1–4], which may be pertinent to the matter-antimatter asymmetry of our universe [5]. As a result, there would be more particles with one certain chirality than the other, which is called chirality imbalance. If there is a strong magnetic field, the spins of particles would be locked either parallel or antiparallel to the magnetic field direction, depending on their charges. Then, with the same chirality imbalance and opposite spin directions, the positive and negative charged particles would have opposite momentum directions. This charge separation phenomenon is called the chiral magnetic effect (CME) [6].

In heavy-ion collisions, we refer to the collided nucleons as participants and the others as spectators. From the collision geometry, the magnetic field created by the spectator protons is generally perpendicular to the reaction plane (RP, spanned by the impact parameter and beam direction), so the CME searches usually take RP as the reference direction. The particle distribution can be expanded with respect to (w.r.t.) RP in azimuth (ψ_{RP}) into a Fourier series

$$\frac{2\pi}{N}\frac{dN}{d\phi} = 1 + 2v_1\cos(\phi-\psi_{\mathrm{RP}}) + 2v_2\cos 2(\phi-\psi_{\mathrm{RP}}) + \dots, \tag{1}$$

where N is the number of particles and ϕ is the azimuthal angle in the plane perpendicular to the beam axis.

The charge-dependent azimuthal correlator $\Delta\gamma$ is used to measure the charge separation of CME [7]. Its definition is as follows:

$$\gamma_{\alpha\beta} \equiv \langle\cos(\phi_\alpha + \phi_\beta - 2\psi_{\mathrm{RP}})\rangle. \tag{2}$$

Here, the subscripts α, β represent two different particles of interest (POI) in the same event, and their electric charge signs determine whether the pair ($\alpha\beta$) is opposite sign (OS) or same sign (SS). For a given pair sign (OS or SS), the angle brackets $\langle\cdots\rangle$ represent the average over those pairs within one event and then further averaged over multiple events in each centrality. The signature of CME is that $\gamma_{\mathrm{OS}} > 0$ and $\gamma_{\mathrm{SS}} < 0$ with the same magnitude [7]. However, there are correlation backgrounds that can also cause the γ correlators to deviate from zero [7]. Many of these backgrounds are charge independent, such as those arising from momentum conservation. In order to remove those charge-independent backgrounds, the difference between OS and SS is computed as follows:

$$\Delta\gamma \equiv \gamma_{\mathrm{OS}} - \gamma_{\mathrm{SS}}. \tag{3}$$

Experiments have focused on measuring the $\Delta\gamma$ observable. Large signals of $\Delta\gamma$ have been measured at the Relativistic Heavy-Ion Collider (RHIC) [8–16] and the Large Hadron Collider (LHC) [17–20].

Although charge-independent backgrounds are canceled in $\Delta\gamma$, backgrounds remain from charge-dependent two-particle (2p) correlations coupled with elliptic flow of those correlation sources such as resonance decays and jets [7,21–24]. These backgrounds can be expressed as

$$\gamma_{\mathrm{OS}}^{\mathrm{bkgd}} = \frac{N_{\mathrm{2p}}}{N_{\mathrm{OS}}}\langle\cos(\phi_\alpha + \phi_\beta - 2\phi_{\mathrm{2p}})\rangle_{\mathrm{2p}} v_{2,\mathrm{2p}}. \tag{4}$$

Here, N_{2p}, ϕ_{2p}, and $v_{2,\mathrm{2p}}$ represent the number, azimuthal angle, and elliptic flow parameter of those OS 2p correlation sources (e.g., ρ resonances), respectively. Elliptic flow v_2 is defined as

$$v_2 = \langle\cos(2\phi - 2\psi_{\mathrm{RP}})\rangle, \tag{5}$$

which is also a coefficient in Eq. (1). It has been found that those backgrounds dominate charge-separation measurements [16,24].

To mitigate these backgrounds, STAR conducted experiments of isobar collisions $^{96}_{44}\mathrm{Ru}+^{96}_{44}\mathrm{Ru}$ and $^{96}_{40}\mathrm{Zr}+^{96}_{40}\mathrm{Zr}$ at $\sqrt{s_{NN}} = 200$ GeV in 2018 [25]. The choice of these two isobaric species was based on the strategy of keeping the background constant while changing the signal. It was anticipated that the CME-related signal would be larger in Ru + Ru due to the larger number of protons creating a stronger magnetic field. It was also initially expected that with the same number of nucleons in Zr and Ru, flow-related backgrounds would be the same in the two species' collisions, ideally with charge-independent quantities such as multiplicity and elliptic flow (v_2) the same between the two isobars. However, the STAR data shows a few percent difference between the two isobaric species for both quantities. This discrepancy arises because Ru and Zr have different nuclear sizes and structures, which were predicted by energy density functional theory (DFT) calculations [26–28]. For the charge-dependent and CME-sensitive quantity, the STAR data show the isobar ratio (Ru + Ru/Zr + Zr) of $\Delta\gamma/v_2$ below unity [25]. This seems opposite to the initial expectation of larger CME in Ru + Ru but, in fact, results from the different multiplicities. If the number of background correlation sources is proportional to multiplicity (N), then background $\Delta\gamma$ would be diluted by N because $\Delta\gamma$ is a pairwide average and the pair multiplicity $N_{\rm OS}, N_{\rm SS} \propto N^2$. Then, the naive background baseline of $\frac{(\Delta\gamma/v_2)^{\rm Ru}}{(\Delta\gamma/v_2)^{\rm Zr}}$ would be $\frac{(1/N)^{\rm Ru}}{(1/N)^{\rm Zr}}$, and Ref. [25] finds that the former is larger than the latter, though with large uncertainties, suggesting a small CME signal [29].

However, this $1/N$ scaling for $\Delta\gamma/v_2$ is approximate. It assumes that the number of background sources is proportional to multiplicity, $N_{\rm 2p} \propto N$. This assumption may not hold for the two isobar collision systems and may be violated differently in the two due to their slightly different energy densities. A more precise way of scaling may be to divide $\Delta\gamma/v_2$ by $r = N_{\rm 2p}/N_{\rm OS}$ (Sec. III A). Then, the STAR data show the isobar ratio of $\frac{1}{r}\Delta\gamma/v_2$ below unity [25], indicating more complications to be considered [30]. The fact that scaling by r does not give the same result as scaling by multiplicity indicates that the assumption of proportionality is not necessarily valid—there are residual backgrounds in addition to the naive baseline of unity.

Consequently, it is critical to pin down the exact background baseline in order to access information on the CME from the $\Delta\gamma$ measurements in isobar collisions. It is the goal of this paper and Ref. [31] to arrive at a rigorous estimate of the background baseline and examine what the isobar data entail with respect to the possible CME signal. Reference [31] summarizes the essential findings, and this paper provides necessary details of the analysis work.

II. BACKGROUND BASELINE

In heavy-ion experiments, RP is unknown. One often reconstructs an event plane (EP) from the particle momentum distribution, taking this reconstructed EP as a proxy for RP. More elegantly, one exploits particle cumulants; instead of reconstructing an EP, one can calculate v_2 from the two-particle correlator

$$v_2^* = \sqrt{\langle \cos 2(\phi_\alpha - \phi_\beta)\rangle}. \tag{6}$$

This v_2 measurement includes nonflow backgrounds, such as two-particle correlations from jets or resonance decays, whose contribution we quantify by

$$\epsilon_{\rm nf} = \frac{v_{2,\rm nf}^2}{v_2^2} = \frac{v_2^{*2}}{v_2^2} - 1. \tag{7}$$

Here, v_2^* stands for the measurement that includes nonflow correlations unrelated to the global collision geometry, while v_2 refers to the true flow. Note that the cumulant measurement of v_2^* is similar to that obtained by reconstructing an EP, but with subtle differences [32,33]. It should also be noted that the elliptic flow measured by the EP method is also contaminated by nonflow, as the EP is reconstructed using final-state particles [34]. However, the decomposition of nonflow from flow in the EP method is less straightforward than that in the cumulant method [35].

Similarly, instead of calculating the γ correlation using Eq. (2), one can measure a three-particle (3p) correlator

$$C_{3,\alpha\beta} = \langle \cos(\phi_\alpha + \phi_\beta - 2\phi_c)\rangle. \tag{8}$$

Here, c represents a third particle that is different from α, β. The γ correlator can be calculated using $\gamma_{\alpha\beta} = C_{3,\alpha\beta}/v_{2,c}$, where $v_{2,c}$ is the elliptic flow of particle of type c, given by Eq. (5). Effectively, particle c serves as the event plane, and its resolution is simply equal to the particle's elliptic flow $v_{2,c}$. In practice, γ is determined by dividing by the measured quantity v_2^*,

$$\gamma_{\alpha\beta} = C_{3,\alpha\beta}/v_2^*. \tag{9}$$

The main background in C_3 ($=C_{3,\rm OS} - C_{3,\rm SS}$) arises from the flow-induced background [16,24]. In this scenario, some of the POI's are correlated with one another via a 2p source and these 2p sources are all correlated with each particle c through the global flow correlation. This flow-induced background is described by Eq. (4). In addition to this flow-induced background, there is contamination in C_3 from genuine 3p correlations, where the three particles α, β, and c are intrinsically correlated. Thus, the background contributions to the 3p correlators can be expressed as:

$$\begin{aligned} C_{3,\rm OS}^{\rm bkgd} &= \frac{N_{\rm SS}}{N_{\rm OS}}\gamma_{\rm SS} v_{2,c} + \frac{N_{\rm 2p}}{N_{\rm OS}} C_{\rm 2p,OS} v_{2,\rm 2p} v_{2,c} + \frac{N_{\rm 3p,OS}}{N_{\rm OS}N_c} C_{\rm 3p,OS}, \\ C_{3,\rm SS}^{\rm bkgd} &= \gamma_{\rm SS} v_{2,c} + \frac{N_{\rm 3p,SS}}{N_{\rm SS}N_c} C_{\rm 3p,SS}, \end{aligned} \tag{10}$$

where the first terms in both lines are the charge-independent backgrounds, such as momentum conservation, which will be largely canceled out when taking OS − SS. The shorthand notations stand for

$$\begin{aligned} C_{\rm 2p,OS} &= \langle \cos(\phi_\alpha + \phi_\beta - 2\phi_{\rm 2p})\rangle_{\rm 2p,OS}, \\ C_{\rm 3p,OS} &= \langle \cos(\phi_\alpha + \phi_\beta - 2\phi_c)\rangle_{\rm 3p,OS}, \\ C_{\rm 3p,SS} &= \langle \cos(\phi_\alpha + \phi_\beta - 2\phi_c)\rangle_{\rm 3p,SS}, \end{aligned} \tag{11}$$

where the average $\langle\cdots\rangle_{\rm 2p,OS}$ runs only over the correlated background pairs with parent cluster azimuth $\phi_{\rm 2p}$. The averages $\langle\cdots\rangle_{\rm 3p,OS}$ and $\langle\cdots\rangle_{\rm 3p,SS}$ run over only the correlated background triplets, whose multiplicities are $N_{\rm 3p,OS}$ and $N_{\rm 3p,SS}$, respectively. In other words, these quantities characterize the angular properties of the correlated clusters and are not diluted by combinatorial multiplicities. In Eq. (10), the set of OS pairs consists of two components: the first component is the correlated 2p OS pairs, while the second component comprises the remaining OS pairs that are identical to the SS pairs (in terms of the γ quantity). The number of correlated 2p pairs is denoted by $N_{\rm 2p} = N_{\rm OS} - N_{\rm SS}$. The correlated 3p triplets also contribute nonflow background to $\Delta\gamma$ and are treated as a separate term in Eq. (10). It is worth noting that the v_2's in Eq. (10) are the true elliptic flows, as they arise from the correlations between the common global symmetry of the correlated 2p source ($v_{2,\rm 2p}$) and the particle c ($v_{2,c}$), giving rise to the contribution to C_3. In this study, $v_{2,c} = v_2$ because the c particles use the same cut as POI.

The γ correlators are calculated from C_3 by Eq. (9). The backgrounds in $\Delta\gamma/v_2^*$ can be expressed using Eq. (10) as

$$\frac{\Delta\gamma_{\text{bkgd}}}{v_2^*} = \frac{C_{2\text{p}}}{N}\cdot\frac{v_2^2}{v_2^{*2}} + \frac{C_{3\text{p}}}{N}\cdot\frac{1}{N_c v_2^{*2}}. \quad (12)$$

The first term comes from the two-particle (2p) nonflow backgrounds (such as resonance decay daughter pairs, and OS pairs from intra-jet correlation)

$$\frac{C_{2\text{p}}}{N} = \frac{N_{2\text{p}}}{N_{\text{OS}}}\left(C_{2\text{p,OS}}\frac{v_{2,2\text{p}}}{v_2} - \frac{\gamma_{\text{SS}}}{v_2}\right), \quad (13)$$

where $v_{2,2\text{p}}$ is the elliptic flow parameter of the correlated pairs (such as resonance decays). The second term arises from the three-particle (3p) nonflow backgrounds, such as jets

$$\frac{C_{3\text{p}}}{N} = \frac{N_{3\text{p,OS}}}{N_{\text{OS}}}C_{3\text{p,OS}} - \frac{N_{3\text{p,SS}}}{N_{\text{SS}}}C_{3\text{p,SS}}, \quad (14)$$

where the N is the multiplicity of POI, and N_c is that of particle c (in this analysis $N = N_c$). Both the Eqs. (13) and (14) have their corresponding SS contributions subtracted from their OS components, as how $\Delta\gamma$ is defined.

With this decomposition, the isobar ratio due to these background sources can be calculated for $\Delta\gamma/v_2^*$. After approximation to the leading order, the expression becomes

$$\begin{aligned} Y_{\text{bkgd}} &\equiv \frac{(\Delta\gamma_{\text{bkgd}}/v_2^*)^{\text{Ru}}}{(\Delta\gamma_{\text{bkgd}}/v_2^*)^{\text{Zr}}} \\ &\approx 1 + \frac{\delta(C_{2\text{p}}/N)}{C_{2\text{p}}/N} - \frac{\delta\epsilon_{\text{nf}}}{1+\epsilon_{\text{nf}}} \\ &\quad + \frac{1}{1+\frac{Nv_2^2}{C_{3\text{p}}/C_{2\text{p}}}}\left(\frac{\delta C_{3\text{p}}}{C_{3\text{p}}} - \frac{\delta C_{2\text{p}}}{C_{2\text{p}}} - \frac{\delta N}{N} - \frac{\delta v_2^2}{v_2^2}\right), \end{aligned} \quad (15)$$

where $\delta X \equiv X^{\text{Ru}} - X^{\text{Zr}}$ for any $X = C_{3\text{p}}, C_{2\text{p}}$, etc., while all other quantities without "δ" refer to those in Zr + Zr.

We note that the details of 2p and 3p correlation sources can be complicated. For example, besides two- and three-body decays of resonances, they can also come from multiparticle decays of clusters or jets. The OS and SS background pairs, besides the extra OS pairs from decays of neutral objects, may still not be strictly symmetric (e.g., decays from the Δ resonances). In addition, the decay kinematics themselves can be altered in heavy-ion collisions, such as by the possible global spin alignment of ρ mesons [36]. Our analysis formalisms, however, do not rely on those details, but only on the overall OS–SS difference in the γ correlators and the overall nonflow contribution to v_2^*.

III. ANALYSIS

In order to estimate the background baseline, we need to analyze the isobar data to assess the quantities required by Eq. (15). Since the purpose is to estimate the background in the measurements of the STAR isobar blind analysis, we use the same data sets, follow the same event and track selections, and apply identical analysis cuts as described in Ref. [25].

The majority of the analysis cuts are the same for all $\Delta\gamma/v_2$ measurements in the blind analysis. These are as follows: On the event level, the minimum-bias trigger is used—correlated hits in both vertex position detectors (VPD) within a time window. The primary vertex reconstructed by the time projection chamber (TPC) [37,38] is also required to have a longitudinal z position between −35 cm and 25 cm ($-35 < V_z < 25$ cm) and a transverse position to be within 2 cm ($V_\perp < 2$ cm) with respect to the center of TPC. In addition, the interaction position measured online by the vertex position detector (VPD) [39] is required to be within 5 cm from the reconstructed primary vertex along the beam ($|V_z - V_z^{\text{VPD}}| < 5$ cm). On the track level, the reconstructed particle tracks must have more than 15 space points measured in the TPC. As the CME is a signal in primordial particles, the track's distance of closest approach to the primary vertex (DCA) is required to be less than 3 cm (DCA < 3 cm). The particle transverse momentum is restricted within $0.2 < p_T < 2$ GeV/c. The pseudorapidity range is limited within $|\eta| < 1$ for the full-event analyses. For the sub-event analyses, where the event is divided into two sub-events based on their η ranges, the measurements in the STAR blind analysis used slightly different ranges. However, for the estimates reported in this paper, all sub-event measurements used the same η ranges; specifically, $-1 < \eta < -0.1$ was considered as the east sub-event, and $0.1 < \eta < 1$ was considered as the west sub-event. The centrality is defined by the number of tracks in the rapidity range $-0.5 < \eta < 0.5$.

In the STAR blind analysis of the isobar data [25], a total of seven $\Delta\gamma/v_2$ measurements were performed by four research groups. Among these measurements, four utilized the two-particle cumulant method for the v_2 measurement and the three-particle cumulant method for the $\Delta\gamma$ measurement. The remaining three measurements used the event-plane method. While both the cumulant and event-plane methods produced similar results, the event-plane method posed significantly more challenges in distinguishing and accounting for nonflow contributions compared to the cumulant method, as aforementioned. For this reason, we concentrate on the former four measurements, namely, the full-event measurements from Group-2 and Group-3, and the sub-event measurements from Group-2 and Group-4. The analysis details of the four measurements differ slightly, and those details are tabulated in the first block of Table II for the corresponding measurements. In our background baseline estimates for the four measurements, we maintain consistency by using the identical analysis cuts for each corresponding measurement. The block in Table II also includes the results for the average over the 20–50% centrality range for the isobar ratios of $\Delta\gamma/v_2$, denoted as $Y \equiv \langle\frac{(\Delta\gamma/v_2)^{\text{Ru}}}{(\Delta\gamma/v_2)^{\text{Zr}}}\rangle$, which were obtained from the STAR blind analysis [25]. The average of each term in Eq. (15) over centrality bins is calculated separately using the inverse statistical uncertainty squared as weight, and then summed together to get the background baseline.

Equation (15) suggests categorizing the nonflow contributions to the background into three ingredients: (i) $\delta(C_{2\text{p}}/N)/(C_{2\text{p}}/N)$, which characterizes the relative difference of flowing clusters between the two isobars; (ii) differences that arise from using v_2^* rather than true flow in the calculation of $\Delta\gamma$, characterized by ϵ_{nf}; and (iii) differences in the relative

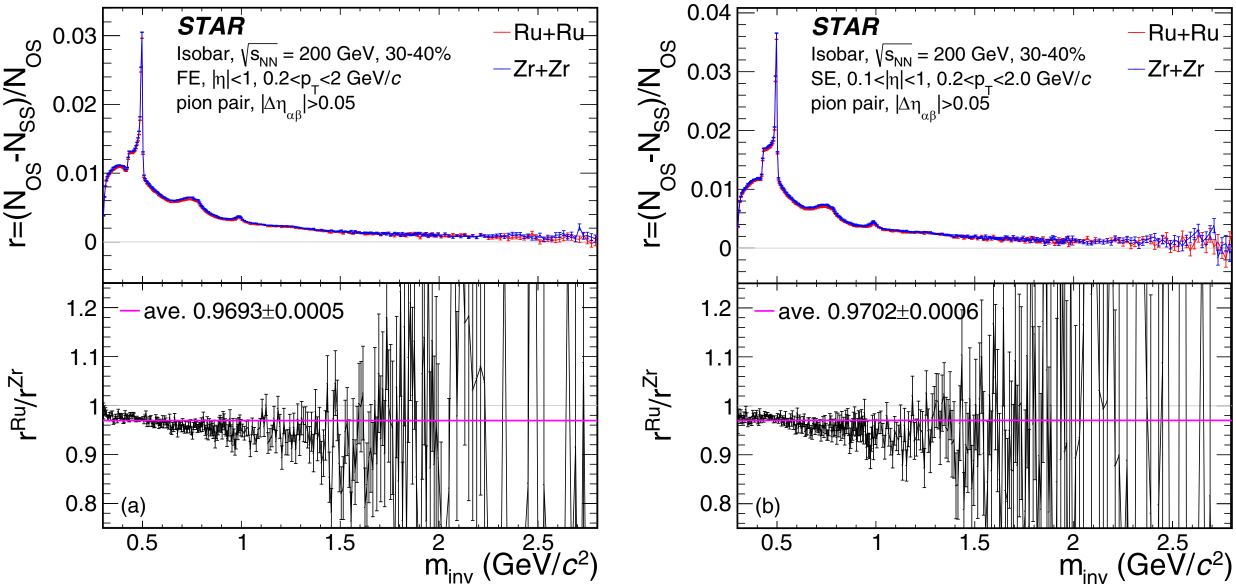

FIG. 1. The relative excess of OS over SS pion pair multiplicity, $r = (N_{\rm OS} - N_{\rm SS})/N_{\rm OS}$, as a function of the pair invariant mass ($m_{\rm inv}$) for the 30–40% centrality in Ru + Ru and Zr + Zr collisions (top panels). The bottom panels show the ratio of r in Ru + Ru to that in Zr + Zr collisions. Full-event results are shown on the left, corresponding to the Group-3 analysis cuts. Sub-event results are shown on the right, corresponding to the Group-2 analysis cuts. Only statistical uncertainties are shown. The pion pair is required to have an η gap $\Delta\eta_{\alpha\beta} > 0.05$. For subevent method, the pion pair needs to come from the same sub-event.

amounts (or character) of three particle clusters between the isobars. In the next section we will discuss each of these three in turn.

A. Pair versus single multiplicity difference

The main background in a $\Delta\gamma$ measurement comes from the charge-independent correlated pairs, such as resonance decays and intra-jet correlations. The number of those pairs is denoted as $N_{\rm 2p} = N_{\rm OS} - N_{\rm SS}$, the excess of OS pairs over SS, so the charge-independent part is removed (similar to $\Delta\gamma = \gamma_{\rm OS} - \gamma_{\rm SS}$). The relative excess is

$$r = \frac{N_{\rm 2p}}{N_{\rm OS}} = \frac{N_{\rm OS} - N_{\rm SS}}{N_{\rm OS}}. \tag{16}$$

This is reflected in the background contribution to $\Delta\gamma$ of Eq. (15).

The $C_{\rm 2p}$ in Eq. (15) refers to the background contribution, and the most relevant quantity is $\delta C_{\rm 2p}$. The zero degree calorimeter (ZDC) [40] measurement of $N\Delta\gamma/v_2$ is close to the background $C_{\rm 2p}$ because the possible CME signal is small and ZDC has a large η gap with TPC (Sec. III C). However, the difference in CME signal contributions in $\delta C_{\rm 2p}$ between the isobar systems may not be negligible compared to that in the background contributions, which is what we need for the baseline estimation. Therefore, we cannot simply take the difference between the ZDC measurements in Ru + Ru and Zr + Zr collisions. Even without this complication, due to the low resolution of the ZDC event plane, the statistical uncertainties of the ZDC $C_{\rm 2p}$ measurements are too large for the precision needed to achieve the background baseline estimate. Therefore, we go to the $C_{\rm 2p}/N$ term itself as defined in Eq. (13). The $C_{\rm 2p,OS}$ represents average angular correlations per 2p cluster (determined by decay kinematics in the case of a resonance decay), and is therefore insensitive to the collision species. The v_2's should well scale between various particle/cluster types. The $\gamma_{\rm OS}/v_2$ is relatively insignificant compared to $C_{\rm 2p,OS}$. It is therefore reasonably safe to assume that the quantity in the parentheses of Eq. (13), i.e., $(C_{\rm 2p,OS}\frac{v_{2,\rm 2p}}{v_2} - \frac{\gamma_{\rm SS}}{v_2})$, is the same for Ru + Ru and Zr + Zr. Thus, we have

$$\frac{\delta(C_{\rm 2p}/N)}{C_{\rm 2p}/N} \approx \frac{\delta r}{r}. \tag{17}$$

In this analysis, we only use pions to calculate r, because the main source of this background is the ρ meson decay and the baryon stopping effect does not affect the produced pions. To identify a track as a pion, the TPC reconstructed track is required to match with a time-of-flight (TOF) detector [39] hit, and additional selections are the TPC energy loss deviation $n\sigma_\pi < 3$, TOF mass $m^2 < 0.1\ {\rm GeV}^2/c^4$, and transverse momentum $0.2 < p_T < 1.8\ {\rm GeV}/c$. To study the invariant pair mass ($m_{\rm inv}$) dependence, r is calculated as a function of $m_{\rm inv}$ (Fig. 1) for Ru + Ru and Zr + Zr separately, and then the isobar ratio is taken between the two. A constant fit is used to extract the average of the ratio. By applying the same procedure to each centrality bin, we can get their centrality dependence as shown in Fig. 2.

The quantity in the parentheses of Eq. (13), assumed to be equal between the two isobar systems, may have a $m_{\rm inv}$ dependence. $Y_{\rm bkgd}$ therefore can be described by the average $\delta r/r$ weighted by a $m_{\rm inv}$-dependent function. We estimate the systematic uncertainty by the variation in r obtained by changing the fit range to $m_{\rm inv} < 1\ {\rm GeV}/c^2$. The resultant difference from the default is expanded to be symmetric and assigned as part of the systematic uncertainty. This is listed

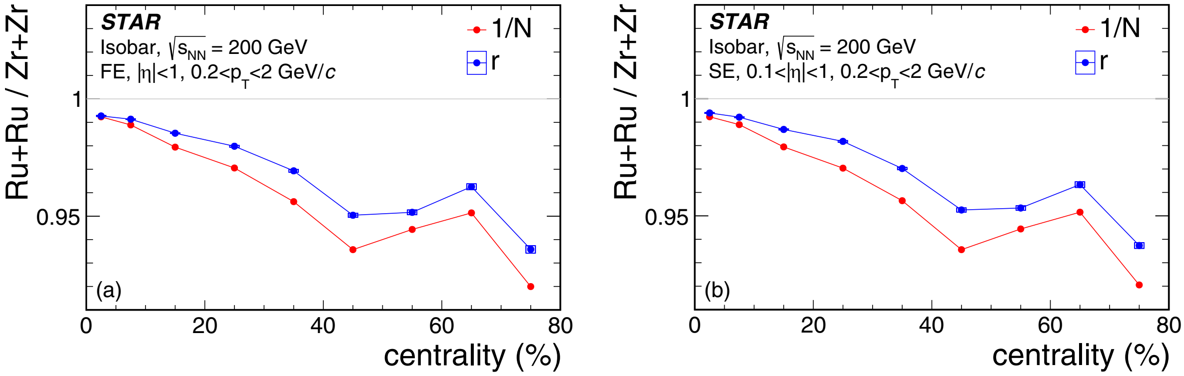

FIG. 2. The Ru + Ru to Zr + Zr ratio of $r = (N_{\mathrm{OS}} - N_{\mathrm{SS}})/N_{\mathrm{OS}}$ and that of the efficiency-corrected inverse multiplicity $1/N$ as functions of centrality for full-event (left panel, with Group-3 cuts) and sub-event (right panel, with Group-2 cuts) methods. Vertical bars are statistical uncertainties; hollow boxes on r data points are systematic uncertainties.

in Table I together with other main sources of systematic uncertainties.

The isobar ratio of $1/N$ is also plotted in Fig. 2, which is different from the isobar ratio of r as mentioned in Sec. I and observed in Ref. [25]. This difference arises from the fact that the background source multiplicity (such as the ρ mesons) does not scale identically with multiplicity for Ru + Ru and Zr + Zr collisions. As a result, the background does not strictly scale as the inverse multiplicity, and thus Y_{bkgd} deviates from unity. The amount of deviation is the difference between the two curves in each panel of Fig. 2.

B. Nonflow contamination in v_2^* measurements

The two-particle correlation is usually used to calculate the elliptic flow in the TPC. However, this method cannot avoid nonflow backgrounds that also correlate with those two particles. To separate the true flow from this inclusive measurement, a data-driven approach is used in this analysis. We fit the two-dimensional (2D) two-particle ($\Delta\eta$, $\Delta\phi$) distribution, where $\Delta\eta$ is the pseudorapidity difference between the two particles, and $\Delta\phi$ azimuth difference. Since the global anisotropy, flow, is supposed to be charge independent, the OS and SS pairs should have the same true flow. We only focus on the SS pairs to avoid the charge-dependent backgrounds that are stronger than charge-independent ones. We assume the true flow is η independent at $|\eta| < 1$, so we only consider the full event method in this section, and use the same fitted flow value to treat the sub-event method. To avoid confusion, we will use "fitted flow" or "fitted v_2" to refer to our estimate, which should closely reflect the underlying true flow.

In the range, $|\eta| < 1$, the single particle η distribution is roughly uniform. Therefore, the $\Delta\eta$ projection of the 2D distribution is mainly a triangle due to the finite η range. This acceptance effect also happens in mixed events. Each pair has one particle from the current event and the other from another similar event (in the same centrality bin, same V_z bin of width 1 cm). However, all other correlations do not exist in those mixed events. Thus, we use the 2D distribution from mixed events, with its peak at $\Delta\eta = 0$ scaled to one, to correct the acceptance effect in real events by taking the ratio of the real over mixed. We assume that the fitted flow does not have a $\Delta\eta$ dependence, so this operation does not affect the fitted flow measurement.

After this acceptance correction, the $\Delta\eta$ distribution generally appears flat, revealing the fine structures of nonflow [shown in Figs. 3(a) and 3(d)]. For each centrality bin, we can get such a corrected 2D distribution, where we see some nonphysical kinks at $|\Delta\eta| = 1 \pm 0.5$. The centrality of this STAR dataset is defined by the charged particle multiplicity within $|\eta| < 0.5$ [25,41]. On the other hand, the POI in this analysis are within $|\eta| < 1$. This distinction means that the centrality bin implicitly imposes an additional constraint on the particle number within $|\eta| < 0.5$ but not for $0.5 < |\eta| < 1$. Consequently, these differences cause those artificial kinks. To eliminate this effect, we project the corrected 2D distribution to $\Delta\eta$ from the away side range of $0.8\pi < |\Delta\phi| < \pi$,

TABLE I. The main sources of systematic uncertainties in Y_{bkgd}. Those contributions from one-sided variations are expanded to be symmetric in the calculation of systematic uncertainties.

Y_{bkgd} syst. source/variation	Affected quantity	Group-2 FE	Group-3 FE	Group-2 SE	Group-4 SE
$m_{\mathrm{inv}} < 1\,\mathrm{GeV}/c^2$ fit range	r	±0.00061	±0.00061	±0.00055	±0.00052
flow decorrelation ±3%	v_2, ϵ_{nf}	±0.00040	±0.00040	±0.00030	±0.00035
alternative 2D fits	v_2, ϵ_{nf}	±0.00016	±0.00107	±0.00058	±0.00065
possible 5% CME in $C_{2\mathrm{p}}$	$C_{2\mathrm{p}}$	±0.00070	±0.00070	±0.00053	±0.00060
HIJING jet quenching off	$C_{3\mathrm{p}}$	±0.00064	±0.00064	±0.00051	±0.00140

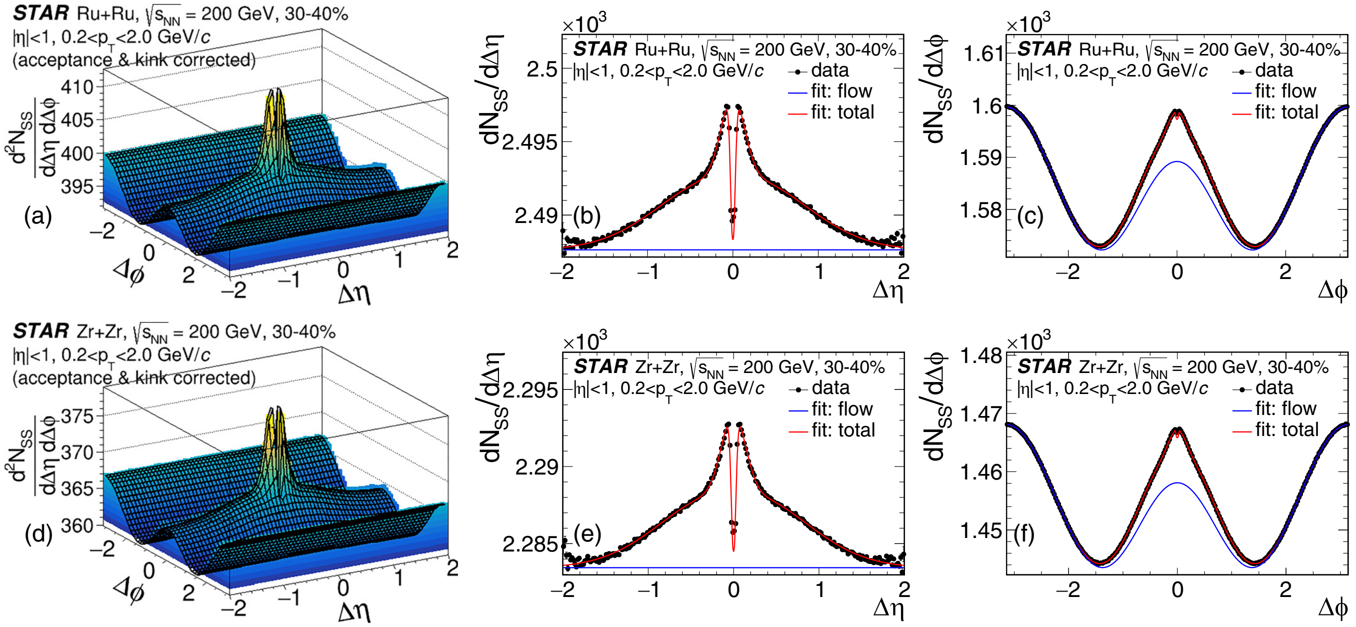

FIG. 3. The left plots show the $(\Delta\eta, \Delta\phi)$ 2D distributions (colored) for SS pairs after acceptance and kink corrections with fit result (black mesh). The middle and right plots are the projections of data (black markers) and fit results (red for total fit function, blue for flow component) to $\Delta\eta$, $\Delta\phi$ directions respectively. The top row is for Ru + Ru and bottom row for Zr + Zr. Only the full-event method and SS pairs are shown here. The fitted flow is assumed to be the same between OS and SS pairs, and the same between full-event and sub-event methods. The centrality range 30−40% is used here, and other centrality ranges are similar.

where the fine structure of nonflow is small and can be ignored. We then subtract its integral from this projection to remove the pedestal, effectively making it a 2D distribution, independent of $\Delta\phi$. By taking the difference between the acceptance-corrected 2D distribution and this projection, we can eliminate the kinks and any ϕ-independent detector effects. It is important to note that this operation does not affect the true flow, as the fitted flow is assumed to be independent of $\Delta\eta$.

With all those operations above, the 2D fit can be conducted, and the fit function from observation and tuning is

$$\begin{aligned} f(\Delta\eta, \Delta\phi) = {} & A_1 G\left(\frac{|\Delta\eta| - \mu}{\sigma_1}\right) G\left(\frac{\Delta\phi}{\rho_1}\right) \\ & + A_2 G\left(\frac{\Delta\eta}{\sigma_2}\right) G\left(\frac{\Delta\phi}{\rho_2}\right) \\ & + \left[A_3 G\left(\frac{\Delta\eta}{\sigma_3}\right) + A_4 G\left(\frac{\Delta\eta}{\sigma_4}\right)\right] G\left(\frac{\Delta\phi}{\rho_3}\right) \\ & + C[1 + 2V_1\cos(\Delta\phi) + 2V_2\cos(2\Delta\phi) \\ & + 2V_3\cos(3\Delta\phi)], \end{aligned} \tag{18}$$

where $G(x) = e^{-x^2/2}$ is the Gaussian function. The second line represents the flow pedestal, and the parameter V_n corresponds to the squared fitted v_n $(n = 1, 2, 3)$ assuming the true flow does not depend on η. The 2D Gaussians are empirical models for nonflow corrections, guided by the data shape [Figs. 3(a) and 3(d)]: track merging effect and Coulomb effect for SS pairs could result in the dip at $\Delta\eta = 0$; HBT, resonance decays, and intra-jet correlations are short range shown by the narrow peak; inter-jet correlations are long range characterized by a wide $\Delta\eta$ Gaussian. In Eq. (18), all the parameters (A, C, V, μ, σ, ρ) are free in the fitting, starting from reasonable initial values. Figure 3 shows the 2D fit results (left) along with their $\Delta\eta$ (middle), $\Delta\phi$ (right) projections in the centrality bin 30–40 % for Ru + Ru (top) and Zr + Zr (bottom) separately.

We note that correlation studies by two-dimensional $(\Delta\eta, \Delta\phi)$ distributions have been performed previously [42–49]. The analysis procedure is well established and produces consistent nonflow contributions. Other analyses to quantify nonflow contributions have also been carried out, for example, by utilizing reflection symmetry in η in symmetric heavy-ion collisions [50], by varying two-particle or sub-event η gap [51–54], and by extrapolating from proton-proton, proton-nucleus, and peripheral heavy-ion collisions to more central collisions assuming inverse multiplicity scaling of nonflow [55].

Figure 4 shows the v_2^{*2} components as functions of centrality for Ru + Ru and Zr + Zr separately. As listed in the legend, this study closely reproduced the previous STAR measurement for v_2^{*2} (Ref. [25], Group-3) using all pairs (OS+SS), the difference is negligible and the numerical difference can be attributed to nonidentical data sets dynamically accessed at run time. The fitted flow is extracted from the SS pair correlations. Thus, the plot also includes the v_2^{*2} measured only from SS pairs, together with the v_2^{*2} calculated from the total fit function, both of which are found to be consistent with each other. Since multiple corrections are applied before conducting the fits, the fit results have been folded back to be comparable to the data. As also shown in the projection plots in Fig. 3, the fitted flow is one component of the total fit

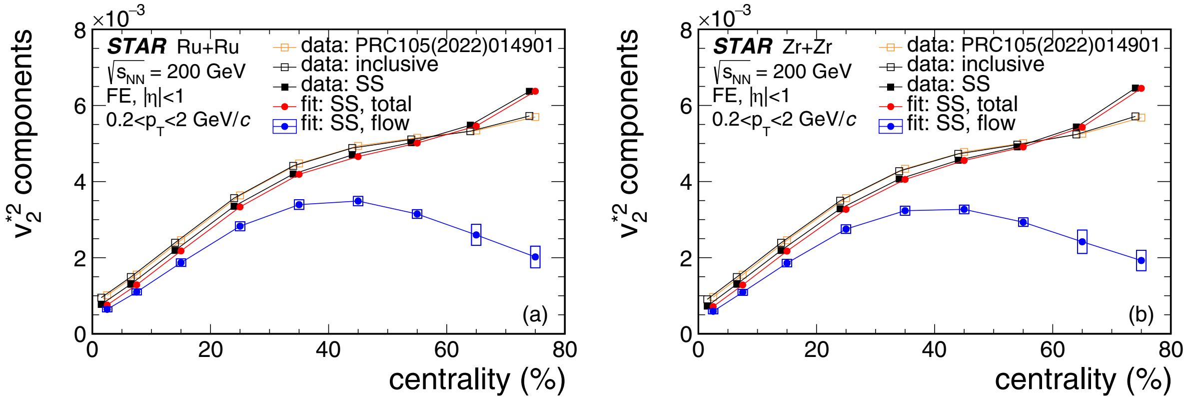

FIG. 4. The v_2^{*2} components as functions of centrality for Ru + Ru (left panel) and Zr + Zr (right panel). The blue curves are the fitted v_2^2. The black and red solid markers are the inclusive v_2^{*2} for SS pairs from data and fit function, respectively, and they agree with each other. The black and orange open squares are the inclusive v_2^{*2} for all pairs from this measurement and the cited Ref. [25] Group-3 (see the plot legends), and they also agree with each other. Vertical bars and hollow boxes show the statistical and systematic uncertainties, respectively.

function, and all the rest are regarded as nonflow components in this study.

The nonflow fraction $\epsilon_{\rm nf}$ can therefore be calculated by Eq. (7) from the fitted flow v_2^2 and the inclusive v_2^{*2} measurements from the STAR isobar blind analysis [25]. Figure 5 presents the $\epsilon_{\rm nf}$ for the two isobars and the isobar difference $\frac{-\delta\epsilon_{\rm nf}}{1+\epsilon_{\rm nf}}$ for both full event and sub-event cases. The boxes represent the systematic uncertainties.

Since the STAR data in Ref. [25] already include the systematics from selection variations, this study does not duplicate them in the baseline estimation to avoid double counting. Instead, it focuses on considering the systematic

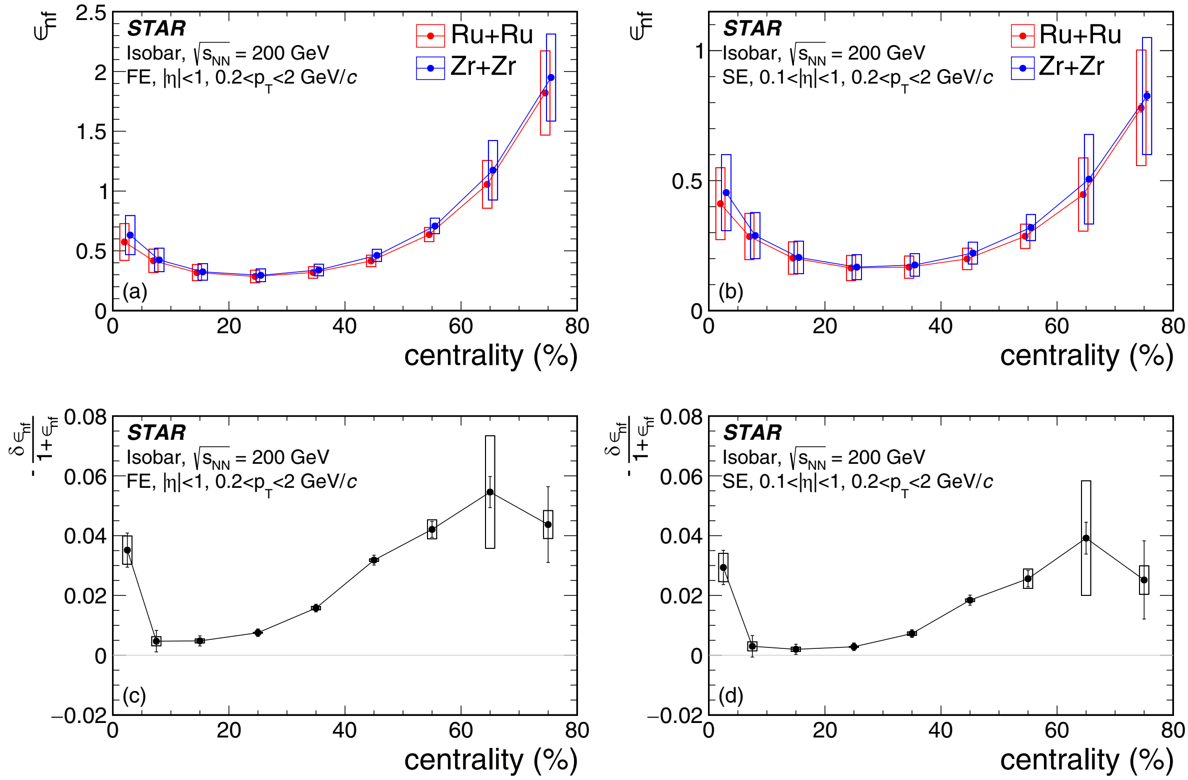

FIG. 5. The relative nonflow strength, $\epsilon_{\rm nf} = v_{2,\rm nf}^2/v_2^2$, in isobar collisions as functions of centrality for full-event data (top left panel, with Group-3 cuts) and sub-event data (top right panel, with Group-2 cuts). The bottom panels depict the corresponding $-\delta\epsilon_{\rm nf}/(1+\epsilon_{\rm nf})$, one of the contributions to the deviation of $Y_{\rm bkgd}$ from unity; see Eq. (15). Vertical bars and hollow boxes show the statistical and systematic uncertainties, respectively.

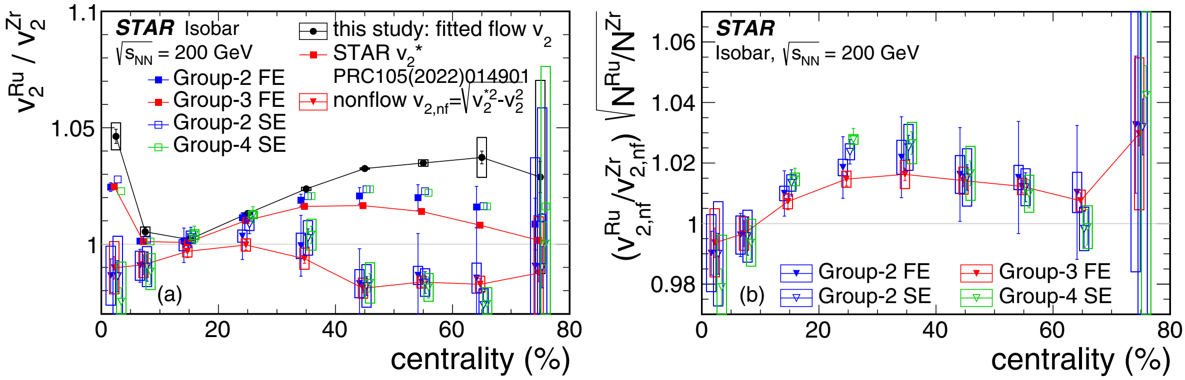

FIG. 6. (Left) The isobar Ru + Ru/Zr + Zr ratio of the fitted v_2 flow parameters as a function of centrality in black solid circles, compared to those of the inclusive v_2^* measurements from the cited STAR isobar blind analysis [25] in colored squares. Full-event (FE) measurements are shown in solid squares, and sub-event (SE) measurements are shown in open squares where the two particles come from two different sub-events. Group-2 (FE) exploited Gaussian fits to reduce nonflow contributions in their measurement, resulting in larger statistical uncertainties and isobar ratios closer to the SE measurements. (Right) The isobar ratio of the extracted nonflow components $v_{2,\mathrm{nf}}$ scaled by the square root of multiplicity as a function of centrality. Vertical bars and hollow boxes show the statistical and systematic uncertainties, respectively. The line connecting one set of the data points is to guide the eye.

uncertainties arising from sources specific to the background baseline estimation of this work. These sources include fit uncertainties and model dependencies. The full-event inclusive v_2^{*2} can be calculated from the 2D distribution (OS+ SS) in this study, represented by the open black curves in Fig. 4. These results are essentially a replication of the measurement conducted by Group-3 in the STAR isobar blind analysis [25], shown as open orange curves in Fig. 4. In addition, a 3% flow decorrelation over one unit of pseudorapidity has been observed [56]. As a result, ±3% variation of v_2^2 is also considered as a systematic uncertainty. Additionally, an alternative 2D fit is used with a different functional form (and corresponding kink correction). The fitted flow deviation from the default is considered as part of the systematic uncertainty. Those systematic sources and their contributions are listed in Table I, where the contributions from onesided variations are expanded to be symmetric in the calculation of systematic uncertainties. It is of interest to examine the relative strength of the fitted flows of the two isobar systems. Figure 6 displays the isobar ratio of the fitted v_2 parameters, where the systematic uncertainties are represented as boxes. The fitted v_2 values averaged over the 20–50% centrality range are 0.0561 ± 0.0010 and 0.0548 ± 0.0010 for Ru + Ru and Zr + Zr collisions, respectively, where the quoted uncertainties are dominated by systematic uncertainties. The average ratio within the 20–50% centrality range is $1.0215 \pm 0.0004(\mathrm{stat.}) \pm 0.0009(\mathrm{syst.})$. The difference in v_2 between the isobar systems originates from variations in the initial collision geometries. These differences can be attributed to distinct nuclear structures, as predicted by DFT calculations [26,28,57]. Both hydrodynamic calculations [58] and transport models [27] can produce the isobar v_2 ratios similar to data, including the subtle hump structure of the ratio in the medium centrality region, once the DFT calculated densities are implemented in those models. The significant difference in the most central collisions arises predominantly from nuclear deformations. For comparison, the isobar ratio of the inclusive v_2^* from STAR data [25] are also plotted in Fig. 6. The measured v_2^* ratios are significantly smaller than those of the fitted, presumably true v_2. This is because nonflow contamination in Ru + Ru is smaller than that in Zr + Zr due to the higher charged particle multiplicity dilution. This is shown in Fig. 6 by the triangles where most data points are below unity. Factoring out the multiplicity dilutions, Fig. 6(b) shows the ratio of $\sqrt{N}v_{2,\mathrm{nf}}$, which reflects the genuine difference in nonflow correlations between the isobar systems. The ratio is in fact larger than unity for most centralities, which is consistent with the presumably larger energy density achieved in Ru + Ru than Zr + Zr collisions.

Azimuthal anisotropies in central heavy-ion collisions are particularly sensitive to nuclear deformations [59,60]. It is noteworthy that the difference between the measured v_2^* ratio and the fitted one is significant also in the most central collisions, as shown in Fig. 6(a). This suggests that using comparisons of the measured v_2^* ratio to hydrodynamic or other model calculations, which often fail to describe nonflow contributions, to infer nuclear deformations should be taken with caution [61,62]. It is interesting to observe that there is no significant difference between full-event and sub-event v_2^* results in the most central collisions. This similarity arises because the relative nonflow contribution to v_2^* is similar between full-event and sub-event for those central collisions, as shown in Fig. 5.

C. Three-particle correlation background

The three-particle (3p) background correlation is the last piece needed to form the background baseline estimate, but it is challenging to measure due to the significant combinatorial background. We resort to the HIJING (Heavy Ion Jet Interaction Generator) model [63,64], which simulates parton-parton hard scatterings based on perturbative QCD

TABLE II. Isobar measurements in the 20–50% centrality range from the STAR blind analysis [25] and the corresponding background baseline estimates from this work, for the four measurements using cumulant analysis techniques (two-particle cumulant for v_2^* and three-particle cumulant for $\Delta\gamma$). Kinematic cuts [25] are $|\eta| < 1$ for full event (FE) and $0.1 < |\eta| < 1$ for sub-event (SE), both with $0.2 < p_T < 2$ GeV/c. The first block lists the important analysis cuts [25], slightly differing among the four measurements, along with the isobar ratios of the $\langle\Delta\gamma/v_2\rangle$ measurements [25] (denoted as Y). The second block tabulates the ingredients used for the background baseline estimates, either from data or HIJING simulations with the corresponding analysis cuts, along with final background baseline (Y_{bkgd}) as well as the magnitudes of its three components in Eq. (15). The last block lists the background subtracted signal (Y_{signal}) and the CME upper limit at the 95% confidence level assuming the CME signal difference between Ru+Ru and Zr+Zr is 15%. The first quoted uncertainty is statistical and the second systematic.

	Group-2 FE	Group-3 FE	Group-2 SE	Group-4 SE
$\Delta\gamma$ cuts	$\lvert\Delta\eta_{\alpha\beta}\rvert > 0.05$		$\lvert\Delta\eta_{\alpha\beta}\rvert > 0.05$	–
v_2^* cuts	$\lvert\Delta\eta_c\rvert > 0.05$ & Gaus. fit	–	–	Same-sign only
$Y \equiv \langle\frac{(\Delta\gamma/v_2^*)^{\text{Ru}}}{(\Delta\gamma/v_2^*)^{\text{Zr}}}\rangle$	$0.9658 \pm 0.0050 \pm 0.0007$	$0.9733 \pm 0.0040 \pm 0.0010$	$0.9611 \pm 0.0070 \pm 0.0016$	$0.9629 \pm 0.0050 \pm 0.0003$
$\langle\epsilon_{\text{nf}}\rangle$	$0.2528 \pm 0.0027 \pm 0.0489$	$0.3419 \pm 0.0008 \pm 0.0555$	$0.1812 \pm 0.0007 \pm 0.0464$	$0.1948 \pm 0.0007 \pm 0.0465$
$\langle C_{\text{2p}}\rangle$ (ZDC)	$0.8302 \pm 0.0511 \pm 0.0415$		$0.5236 \pm 0.0375 \pm 0.0262$	$0.6097 \pm 0.0540 \pm 0.0305$
$\langle C_{\text{3p}}\rangle$ (HIJING)	$0.0707 \pm 0.0005 \pm 0.0084$		$0.0133 \pm 0.0002 \pm 0.0013$	$0.0135 \pm 0.0002 \pm 0.0013$
$\langle\delta C_{\text{3p}}/C_{\text{3p}}\rangle$ (HIJING)	$-0.0054 \pm 0.0102 \pm 0.0049$		$-0.0035 \pm 0.0262 \pm 0.0065$	$-0.0180 \pm 0.0241 \pm 0.0073$
$\langle\delta r/r\rangle$	$-0.0329 \pm 0.0003 \pm 0.0007$		$-0.0308 \pm 0.0004 \pm 0.0006$	$-0.0323 \pm 0.0003 \pm 0.0006$
$\langle-\delta\epsilon_{\text{nf}}/(1+\epsilon_{\text{nf}})\rangle$	$0.0097 \pm 0.0028 \pm 0.0001$	$0.0162 \pm 0.0008 \pm 0.0013$	$0.0080 \pm 0.0008 \pm 0.0007$	$0.0075 \pm 0.0008 \pm 0.0008$
the third term	$-0.0144 \pm 0.0017 \pm 0.0011$		$-0.0108 \pm 0.0028 \pm 0.0008$	$-0.0125 \pm 0.0025 \pm 0.0016$
Y_{bkgd}	$0.9625 \pm 0.0033 \pm 0.0013$	$0.9689 \pm 0.0019 \pm 0.0016$	$0.9664 \pm 0.0029 \pm 0.0011$	$0.9628 \pm 0.0027 \pm 0.0018$
Y_{signal}	$0.0033 \pm 0.0060 \pm 0.0014$	$0.0044 \pm 0.0043 \pm 0.0019$	$-0.0052 \pm 0.0075 \pm 0.0020$	$0.0001 \pm 0.0061 \pm 0.0018$
$f_{\text{CME}}^{\text{Ru}}$ upper limit	11.5%	10.3%	8.3%	9.8%

and gives a reasonable description of partonic energy loss in the QGP medium (jet quenching). Since HIJING does not have collective flow, the correlator $C_3 \equiv C_{3,\text{OS}} - C_{3,\text{SS}}$ in HIJING is entirely composed of genuine three-particle correlations, $C_{3,\text{OS}} = \frac{N_{\text{3p,OS}}}{N_{\text{OS}}N}C_{\text{3p,OS}}$, $C_{3,\text{SS}} = \frac{N_{\text{3p,SS}}}{N_{\text{SS}}N}C_{\text{3p,SS}}$ [cf. Eq. (10)]. The path-length-dependent jet quenching does produce some degree of anisotropy in the final-state particle azimuthal distribution, sensitive to the initial geometry and indistinguishable from collective anisotropy. This anisotropy, however, is negligible compared to the effect of the 3p correlations [65]. The 3p correlation strength, C_{3p}, can be readily obtained from the 3p correlator in HIJING,

$$C_{\text{3p}} = N^2 C_3. \tag{19}$$

We use HIJING v1.411 and simulate 7×10^9 events each for Ru + Ru and Zr + Zr collisions at $\sqrt{s_{NN}} = 200$ GeV. The nuclear structure density distributions are given by energy density functional theory calculations [26–28], and they are implemented in the initial geometry setup in HIJING. Only the final-state charged pions, kaons, protons, and their antiparticles are used for centrality definition and POI. The centrality is defined by the multiplicity distribution of particles with $|\eta| < 0.5$. The same analysis cuts as the STAR isobar data analysis [25] (see Table II) are used to process HIJING simulation data. Figure 7 shows the C_{3p} in isobar collisions as functions of centrality, as obtained from HIJING simulations, and the Ru + Ru over Zr + Zr ratios of C_{3p}. The centrality dependence is weak, as one would expect for C_{3p}, which is defined for the correlated triplets with the dilution effect factored out as in Eq. (14). The C_{3p} is larger in full-event than sub-event because the number of triplets drops with acceptance more rapidly than single multiplicity. An important question is how well HIJING describes data in terms of 3p correlations? The question cannot be directly answered because of the difficulties to access the 3p correlations in real data as aforementioned. However, there are a few checks one can make. We first examine how well HIJING describes the C_3 in peripheral collisions, where the nonflow effects dominate due to smaller multiplicity dilution. We show the measured C_3 in data and in HIJING in Fig. 8 for full-event and sub-event analysis. As shown in Fig. 8, the 70–80% peripheral data are reasonably well described by HIJING. This suggests that the peripheral C_3 data are dominated by 3p correlations, the flow-induced background is small in peripheral collisions. HIJING is a reasonable model for (mini)jet production as well as soft physics via string fragmentation, so it is considered as suitable description for 3p correlations.

The default setup of our HIJING simulations include jet quenching. We also simulate HIJING with jet quenching turned off. The quenching-off C_{3p} is about 20% higher than the quenching-on result, as shown in Fig. 8. We take this difference as the maximum systematic uncertainty on 3p correlation estimate. As another check, we also show in Fig. 8 the HIJING C_3 without cutting on $\Delta\eta_{\alpha\beta}$ (as in the Group-4 data analysis [25]). The difference is small, and we conclude that HIJING with quenching on and off provide a safe estimate of the one-side maximum systematic uncertainty. We thus assign their difference divided by $\sqrt{3}$, assuming a uniform probability for the systematic uncertainty, to be the one standard deviation systematic uncertainty on our 3p correlation background estimate, and expand it to be symmetric, as listed in Table I.

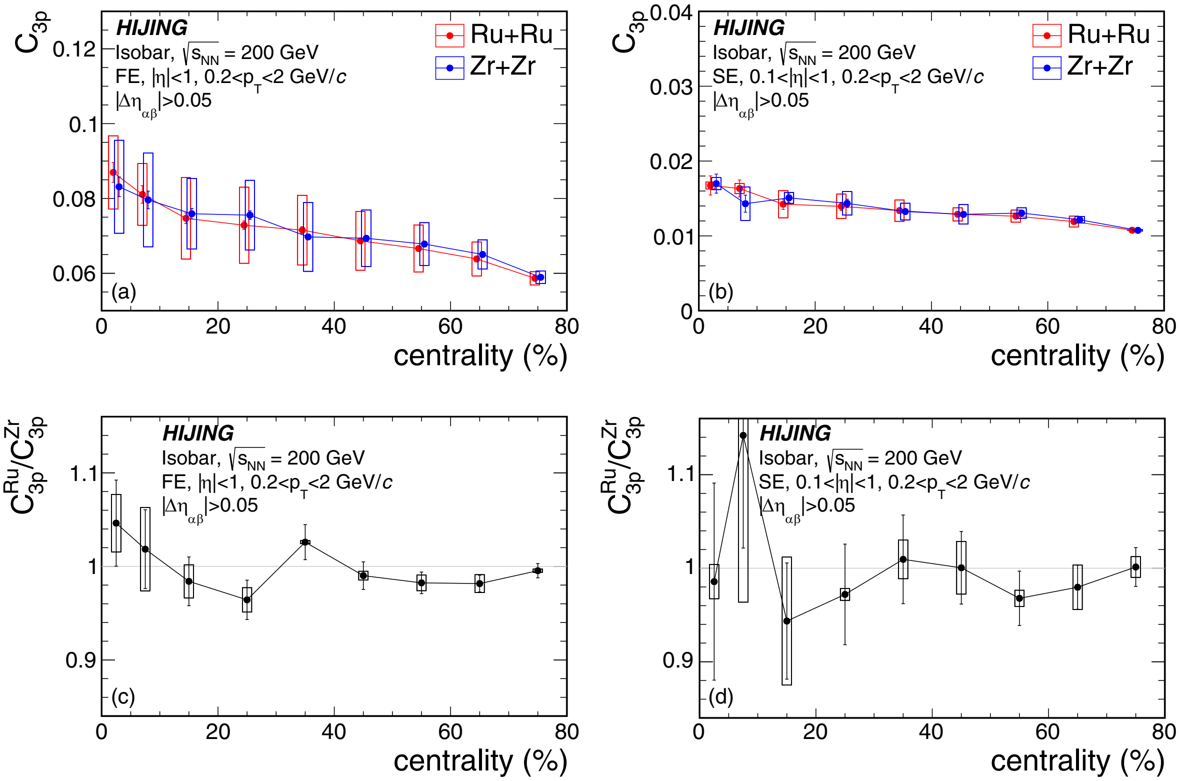

FIG. 7. The C_{3p} in Ru + Ru and Zr + Zr collisions as functions of centrality for full-event (left panel, with Group-3 cuts) and sub-event (right panel, with Group-2 cuts) analysis, obtained from HIJING simulations of 7×10^9 minimum-bias events for each system. The bottom panels show the Ru + Ru over Zr + Zr ratio of C_{3p}. Vertical bars indicate statistical uncertainties. The hollow boxes show systematic uncertainties, estimated from HIJING quenching-off simulations. The two POI's have an η gap, $\Delta\eta_{\alpha\beta} > 0.05$. For the sub-event method, the two POI's come from the same subevent, while the reference particle comes from the other sub-event.

In order to estimate the baseline contribution from 3p correlations, we also need the quantity C_{2p} [Eq. (15)]. As shown in Eq. (13), C_{2p} represents the 2p nonflow background correlations in C_3 measurements. If the azimuth of RP is known, then Eq. (5) gives the true elliptic flow and Eq. (2) gives $\Delta\gamma$ without 3p nonflow by definition. If so, Eq. (12)

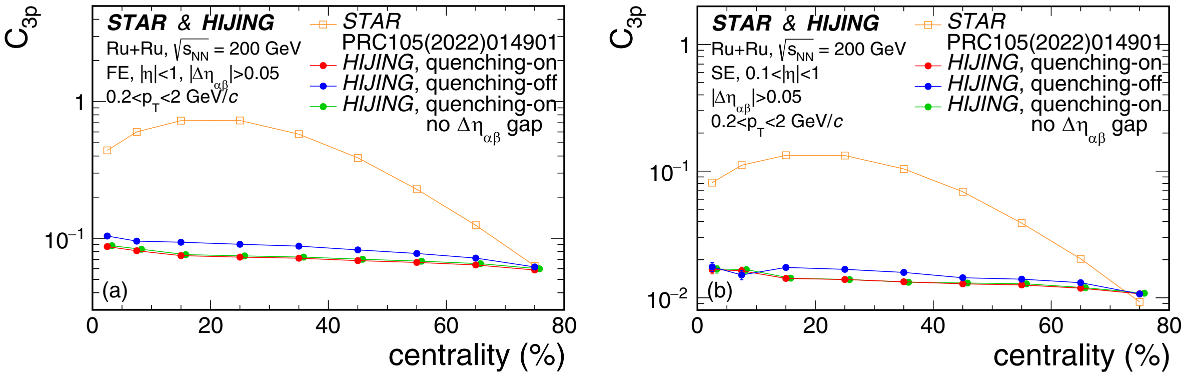

FIG. 8. Comparison of C_{3p} between HIJING (jet quenching on) and the cited STAR measurements [25] in Ru + Ru collisions for full-event (left panel, with Group-3 cuts) and sub-event (right panel, with Group-2 cuts) analyses (Zr + Zr is similar). The data measurements on the plots use Eq. (19), which are inclusive. The peripheral data are similar to the HIJING result, suggesting that the peripheral data are dominated by 3p correlation background. The nonperipheral data are dominated by flow-induced background, absent from HIJING. The C_{3p} results from HIJING simulation with quenching turned off are also shown, which is taken as the maximum systematic uncertainty. The two POI's have an η gap, $\Delta\eta_{\alpha\beta} > 0.05$. For the sub-event method, the two POI's come from the same sub-event, while the reference particle comes from the other sub-event. To give a magnitude assessment, the HIJING (quenching on) results without the $\Delta\eta_{\alpha\beta} > 0.05$ cut (as in Group-4 data analysis [25]) are also displayed.

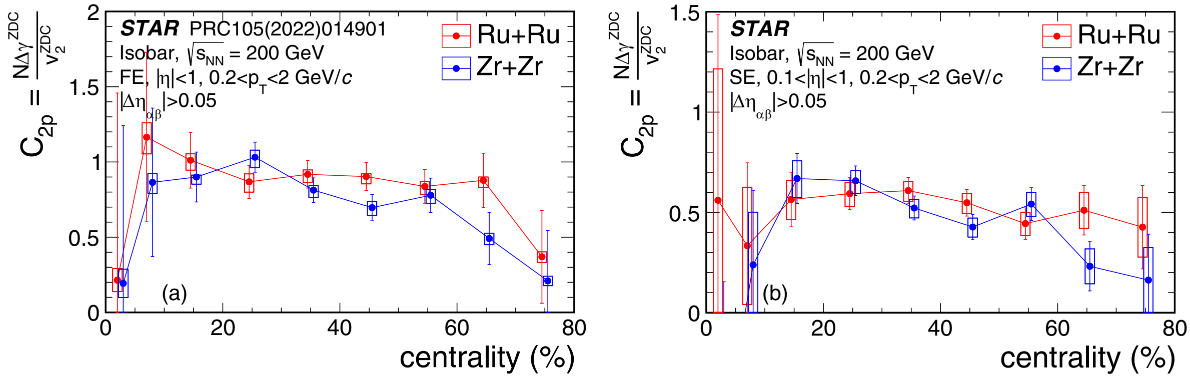

FIG. 9. The C_{2p} in isobar collisions for the full-event (left panel, from the Group-3 isobar result) and sub-event (right panel, with Group-2 cuts) analyses, obtained from the ZDC measurements of $\Delta\gamma/v_2$ multiplied by the efficiency-corrected multiplicity. Vertical bars indicate statistical uncertainties. The asymmetric systematic uncertainty, shown by boxes, is composed of the data systematic uncertainty from the cited Ref. [25] and a one-sided systematic uncertainty of -5% to account for possible CME contributions in the ZDC measurements. The two POI's in $\Delta\gamma$ have an η gap, $|\Delta\eta_{\alpha\beta}| > 0.05$. For subevent method, the POI pair comes from the same sub-event.

simply becomes

$$N\frac{\Delta\gamma_{\rm bkgd}\{\rm RP\}}{v_2\{\rm RP\}} = C_{2p}. \tag{20}$$

In STAR, the ZDC is separated from TPC by a large η gap and at high collision energies measures only spectator neutrons. Thus, the ZDC measurements of the event plane are not correlated with POI, and the $N\Delta\gamma/v_2$ w.r.t. ZDC can be used to estimate C_{2p}. Figure 9(a) shows the full-event ZDC measurement from the STAR isobar blind analysis (Group-3) [25]. Figure 9(b) shows the sub-event ZDC measurement from this analysis because the sub-event ZDC measurement in the STAR blind analysis [25] used $0.05 < |\eta| < 1$ instead of $0.1 < |\eta| < 1$.

The POI multiplicities have been corrected for the centrality- and p_T-dependent track reconstruction efficiencies of the STAR TPC. The average efficiency is on the order of 85%. The efficiency is obtained from Monte Carlo tracks simulated by GEANT in the STAR detector and embedded into the isobar data on the pixel level with proper detector response simulations. In this embedding sample, the input tracks and reconstructed tracks are distributed as functions of centrality, particle species, charge, and p_T, η, which are slightly different between the two isobars. For each centrality bin, we obtain the integral (total number of $p\bar{p}$, $K^\pm$, $\pi^\pm$) inside our cuts (POI) for the reconstructed and input tracks, and their ratio gives us the efficiency. Due to the η gap, the sub-event has slightly different efficiency compared to the full event.

The systematic uncertainties shown in Fig. 9 include those on the ZDC measurements from the blind analysis [25] for both full-event and sub-event analyses. The ZDC measurements could contain some CME signal, possibly on the order of a few percent [16,66]. Because C_{2p} refers to 2p background correlation, we additionally assign a onesided systematic uncertainty of -5% on C_{2p}. This one-sided uncertainty is expanded to be symmetric in the calculation of systematic uncertainties on $Y_{\rm bkgd}$, as listed in Table I. The uncertainties on the ZDC measurement of C_{2p} are not included in those on $Y_{\rm bkgd}$ but only on Y [25], to avoid double counting.

Figure 10 shows the ratios of C_{3p}/C_{2p} as a function of centrality in both full-event and sub-event analyses. The ratios are on the order of a few percent. The ratio in the full event

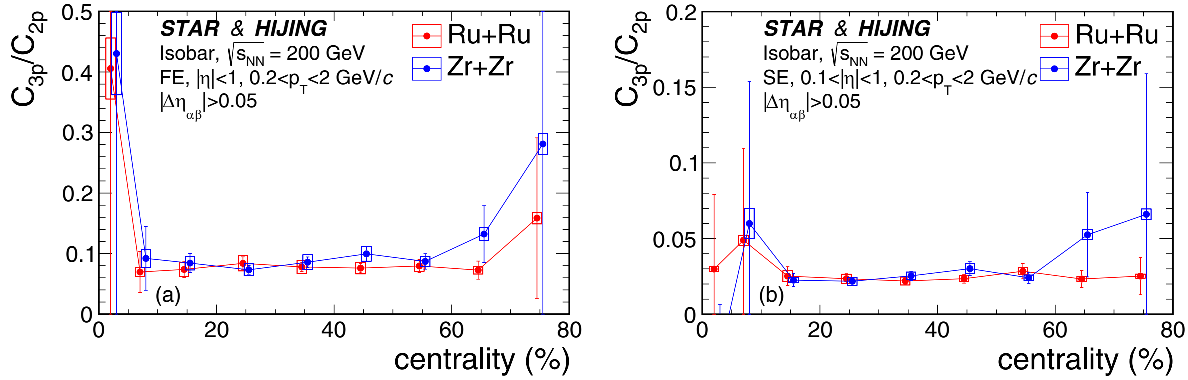

FIG. 10. The ratio C_{3p}/C_{2p} as functions of centrality for full-event (left panel, with Group-3 cuts) and sub-event methods (right panel, with Group-2 cuts). Some of the central and peripheral data points are off the plots with large error bars. Vertical bars and hollow boxes show the statistical and systematic uncertainties, respectively.

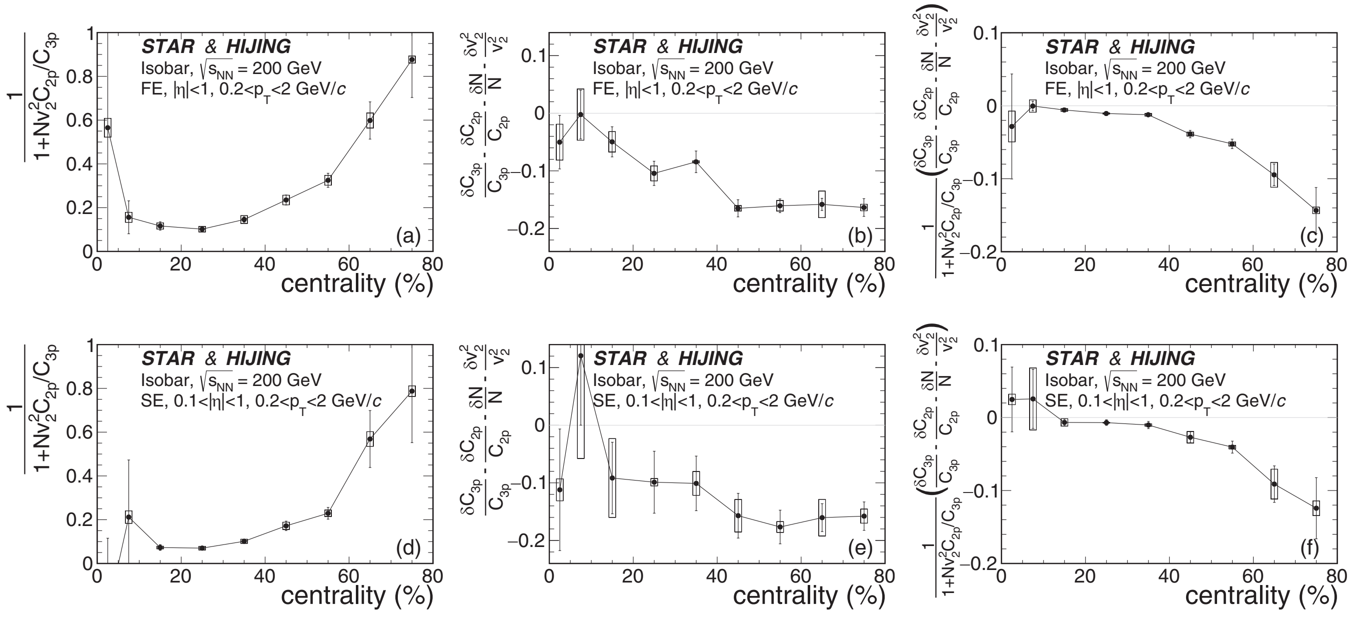

FIG. 11. The nonflow components related to 3p nonflow as functions of centrality for full-event (top row, with Group-3 cuts) and sub-event (bottom row, with Group-2 cuts) methods. The multiplicity N has been corrected for tracking efficiency. Vertical bars and hollow boxes show the statistical and systematic uncertainties, respectively.

is larger than in the sub-event due to a simple acceptance effect—the smaller the acceptance, the smaller the high-order correlations.

With all the ingredients ready, as in Figs. 2, 9, 6, and 7, one can easily calculate the background contribution from 3p correlations. The results are shown in Fig. 11. The prefactor is depicted in the left column, the sum of the various isobar differences is depicted in the middle column, and the final 3p background difference is depicted in the right column.

IV. RESULT

The previous section discusses all the ingredients needed for background estimation. Besides the unity, there are three terms in Eq. (15). These terms are presented in Figs. 2, 5, and 11, separately. The sum of all those terms by Eq. (15) is the background baseline estimate. It is shown in Fig. 12 as a function of centrality, together with the STAR data from Group-3 full-event and Group-2 sub-event measurements. We also apply the same procedure for the other two measurements in the STAR isobar blind analysis [25], namely Group-2 full-event and Group-4 sub-event measurements.

We compute an average background baseline over the centrality range of 20–50%. Each of the three background terms in Eq. (15) is averaged first, weighted by the corresponding inverse squared statistical uncertainty. Then, the three terms are added to yield the average $Y_{\rm bkgd}$ baseline. The average $Y_{\rm bkgd}$ baselines are tabulated in Table II for the four measurements and plotted on the summary plot in Fig. 13.

The difference between the STAR data from Ref. [25] and the baseline from this study, $Y_{\rm signal} = Y - Y_{\rm bkgd}$, reflects the relative isobar difference of the possible CME signals in the

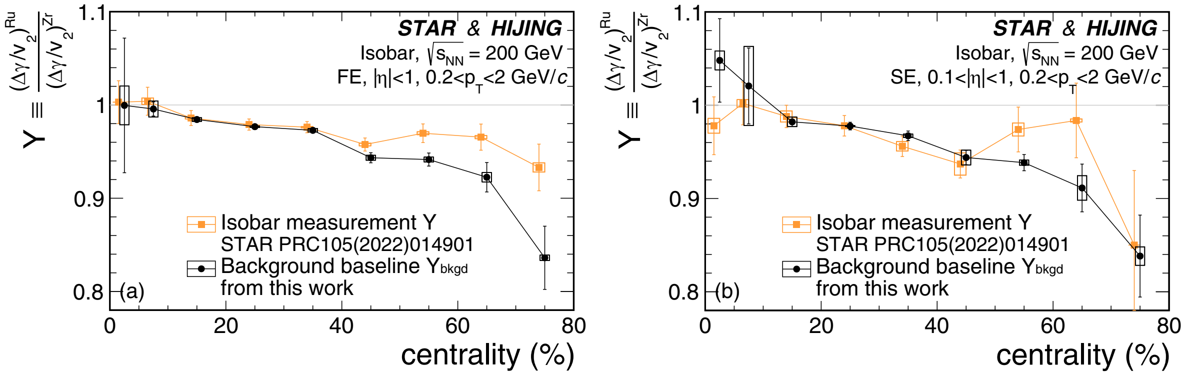

FIG. 12. The $Y \equiv \frac{(\Delta\gamma/v_2^*)^{\rm Ru}}{(\Delta\gamma/v_2^*)^{\rm Zr}}$ measurements from the cited Ref. [25] (orange curves) and background baseline $Y_{\rm bkgd}$ from this study (black curves) as functions of centrality for full-event (left panel, with Group-3 cuts) and sub-event (right panel, with Group-2 cuts) methods. Vertical bars and hollow boxes show the statistical and systematic uncertainties, respectively.

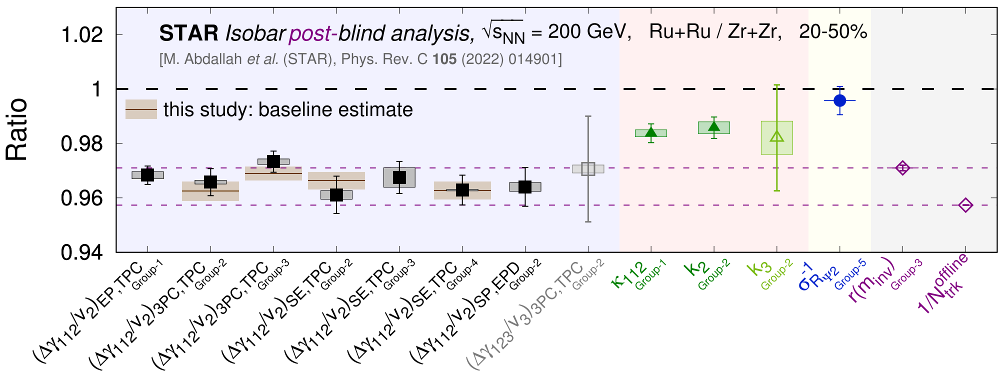

FIG. 13. Compilation of the Ru + Ru to Zr + Zr isobar ratios of the $\Delta\gamma/v_2$ measurements, Y (black squares, with statistical uncertainties indicated by the vertical bars and systematic uncertainties by hollow boxes), and the r and $1/N$ measurements (purple diamonds), with the left coordinate labeling, from the cited STAR blind analysis [25]. The estimated background baselines from this analysis, $Y_{\rm bkgd}$, for the four cumulant measurements of the isobar $\Delta\gamma/v_2$ ratios are shown by the horizontal bars (central values) and the shaded areas (total uncertainties). The total uncertainties are the quadratic sum of the statistical and systematic uncertainties on the background baseline estimates [25].

inclusive $\Delta\gamma$ measurements. Simple algebra indicates

$$Y_{\rm signal} = Y_{\rm bkgd}\frac{\delta f_{\rm CME}}{1-f_{\rm CME}^{\rm Ru}}, \tag{21}$$

where $f_{\rm CME} \equiv \Delta\gamma_{\rm CME}/\Delta\gamma = 1 - \Delta\gamma_{\rm bkgd}/\Delta\gamma$ is the fraction of CME signal in the $\Delta\gamma$ measurement, and $\delta f_{\rm CME} \equiv f_{\rm CME}^{\rm Ru} - f_{\rm CME}^{\rm Zr}$ is its difference between Ru + Ru and Zr + Zr collisions. Assuming the CME signal is proportional to the squared magnetic field, $\Delta\gamma_{\rm CME} \propto B^2$, then after a few steps of algebra we obtain

$$\begin{aligned} f_{\rm CME}^{\rm Ru} &= \frac{Y_{\rm signal}}{Y}\Bigg/\left[1 - Y_{\rm bkgd}\Bigg/\frac{(B^2/v_2^*)^{\rm Ru}}{(B^2/v_2^*)^{\rm Zr}}\right] \\ &\approx \frac{Y_{\rm signal}}{Y}\Bigg/\left[1 - Y_{\rm bkgd}\left(1 + \frac{\delta v_2^*}{v_2^*} - \frac{\delta B^2}{B^2}\right)\right], \end{aligned} \tag{22}$$

where $\delta B^2/B^2 \equiv (B_{\rm Ru}^2 - B_{\rm Zr}^2)/B_{\rm Zr}^2$ is the relative squared magnetic field difference between the isobar collisions. It reduces to the simple relationship $f_{\rm CME}^{\rm Ru} = Y_{\rm signal}/\frac{\delta B^2}{B^2}$ if neglecting small quantities.

Our results for $Y_{\rm signal}$ and $f_{\rm CME}$ are consistent with zero. Assuming $\delta B^2/B^2 = 15\%$ [67,68] and that $f_{\rm CME}$ has a Gaussian probability distribution with a lower bound at the origin [69] ($f_{\rm CME} \geqslant 0$), we extract an upper limit on $f_{\rm CME}^{\rm Ru}$ of roughly 10% for all four measurements at 95% confidence level. (The upper limit on $f_{\rm CME}^{\rm Zr}$ is accordingly smaller.) The upper limits are listed in Table II and illustrated in Fig. 14(a). Figure 14(b) shows the $f_{\rm CME}^{\rm Ru}$ upper limits extracted for a range of values of $\delta B^2/B^2$.

We note that in Fig. 12 the difference between data and baseline in the 50–80% centrality range is $0.0305 \pm 0.0100 \pm 0.0041$ (2.8σ) for full events and $0.0355 \pm 0.0215 \pm 0.0046$ (1.6σ) for sub-events. In the blind analysis [25] and in this work, we have concentrated on the midcentral 20–50% centrality range where the CME is predicted to be more probable than peripheral or central collisions [3,4,6]. We speculate that the peripheral collision results are likely due to fluctuations.

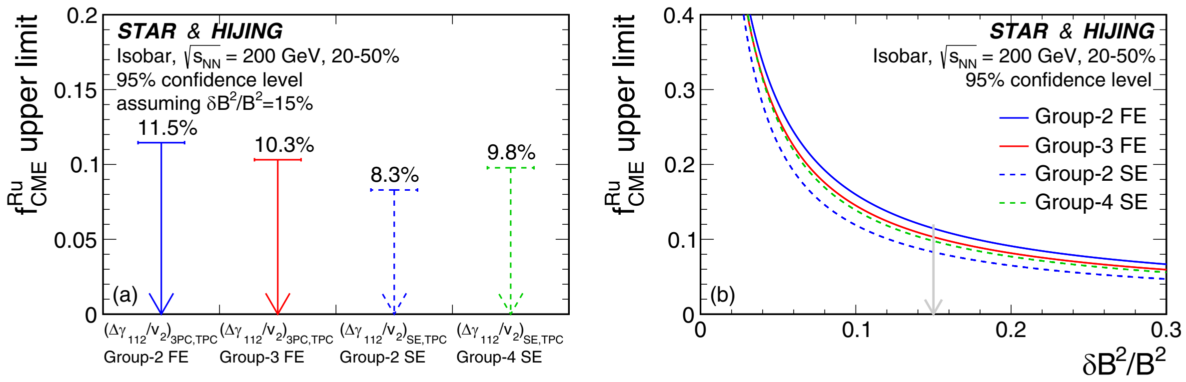

FIG. 14. (Left) Upper limits at 95% confidence level on the CME fraction $f_{\rm CME}^{\rm Ru}$ in the inclusive $\Delta\gamma$ measurement in 20–50% centrality Ru + Ru collisions extracted from the isobar blind analyses [25] with the background baseline estimates for four measurements from this work, assuming a squared magnetic field difference of $\delta B^2/B^2 = 15\%$ between the two isobar systems [67,68]. (Right) Extracted $f_{\rm CME}^{\rm Ru}$ upper limits as a function of $\delta B^2/B^2$. The statistical and systematic uncertainties are added in quadrature in extracting the upper limits.

V. SUMMARY

In this study, we have estimated nonflow contributions in v_2 by fitting two-particle $(\Delta\eta, \Delta\phi)$ distributions and analyzing the deviations from simple multiplicity scaling of the three-particle correlator using the STAR isobar data. The three-particle nonflow correlation contributions to C_3 are evaluated using HIJING simulations. With these inputs, we have obtained an improved background estimate of the Ru + Ru to Zr + Zr ratio of the $\Delta\gamma/v_2$ variable. The estimated background baselines are found to be consistent with the STAR measurements for both the full-event and sub-event methods. We have also extracted an upper limit of the CME fraction of approximately 10% with a 95% confidence level in isobar collisions at 200 GeV.

This paper focuses on the STAR isobar experiments. On the other hand, the Au + Au collision data from STAR indicate a possible finite CME signal [16]. This is consistent with the expectation that the signal-to-background ratio is approximately a factor of three larger in Au + Au collisions than in isobar collisions [66]. To outlook, an order of magnitude increase in statistics is expected from future data taking of Au + Au collisions at 200 GeV [70]. STAR will continue the CME search with those data as well as data from the beam energy scan [71].

ACKNOWLEDGMENTS

We thank the RHIC Operations Group and RCF at BNL, the NERSC Center at LBNL, and the Open Science Grid consortium for providing resources and support. This work was supported in part by the Office of Nuclear Physics within the U.S. DOE Office of Science, the U.S. National Science Foundation, National Natural Science Foundation of China, Chinese Academy of Science, the Ministry of Science and Technology of China and the Chinese Ministry of Education, the Higher Education Sprout Project by Ministry of Education at NCKU, the National Research Foundation of Korea, Czech Science Foundation and Ministry of Education, Youth and Sports of the Czech Republic, Hungarian National Research, Development and Innovation Office, New National Excellency Programme of the Hungarian Ministry of Human Capacities, Department of Atomic Energy and Department of Science and Technology of the Government of India, the National Science Centre and WUT ID-UB of Poland, the Ministry of Science, Education and Sports of the Republic of Croatia, German Bundesministerium für Bildung, Wissenschaft, Forschung and Technologie (BMBF), Helmholtz Association, Ministry of Education, Culture, Sports, Science, and Technology (MEXT), Japan Society for the Promotion of Science (JSPS) and Agencia Nacional de Investigación y Desarrollo (ANID) of Chile.

---

[1] P. D. Morley and I. A. Schmidt, Strong P, CP, T violations in heavy ion collisions, Z. Phys. C **26**, 627 (1985).

[2] D. Kharzeev, R. D. Pisarski, and M. H. G. Tytgat, Possibility of spontaneous parity violation in hot QCD, Phys. Rev. Lett. **81**, 512 (1998).

[3] D. Kharzeev, Parity violation in hot QCD: Why it can happen, and how to look for it, Phys. Lett. B **633**, 260 (2006).

[4] D. E. Kharzeev, L. D. McLerran, and H. J. Warringa, The Effects of topological charge change in heavy ion collisions: 'Event by event P and CP violation', Nucl. Phys. A **803**, 227 (2008).

[5] D. K. Barton, R. Falcone, D. Kleppner, F. K. Lamb, M. K. Lau, H. L. Lynch, D. Moncton, D. Montague, D. E. Mosher, W. Priedhorsky, M. Tigner, and D. R. Vaughan, Origin of the matter-antimatter asymmetry, Rev. Mod. Phys. **76**, S1 (2004).

[6] K. Fukushima, D. E. Kharzeev, and H. J. Warringa, The chiral magnetic effect, Phys. Rev. D **78**, 074033 (2008).

[7] S. A. Voloshin, Parity violation in hot QCD: How to detect it, Phys. Rev. C **70**, 057901 (2004).

[8] B. Abelev *et al.* (STAR Collaboration), Azimuthal charged-particle correlations and possible local strong parity violation, Phys. Rev. Lett. **103**, 251601 (2009).

[9] B. Abelev *et al.* (STAR Collaboration), Observation of charge-dependent azimuthal correlations and possible local strong parity violation in heavy ion collisions, Phys. Rev. C **81**, 054908 (2010).

[10] B. Abelev *et al.*, Charge separation relative to the reaction plane in Pb-Pb collisions at $\sqrt{s_{NN}} = 2.76$ TeV, Phys. Rev. Lett. **110**, 012301 (2013).

[11] L. Adamczyk *et al.*, Fluctuations of charge separation perpendicular to the event plane and local parity violation in $\sqrt{s_{NN}} =$ 200 GeV Au+Au collisions at the BNL Relativistic Heavy Ion Collider, Phys. Rev. C **88**, 064911 (2013).

[12] L. Adamczyk *et al.* (STAR Collaboration), Measurement of charge multiplicity asymmetry correlations in high-energy nucleus-nucleus collisions at $\sqrt{s_{NN}} = 200$ GeV, Phys. Rev. C **89**, 044908 (2014).

[13] L. Adamczyk *et al.* (STAR Collaboration), Beam-energy dependence of charge separation along the magnetic field in Au+Au collisions at RHIC, Phys. Rev. Lett. **113**, 052302 (2014).

[14] J. Adam *et al.* (STAR Collaboration), Charge-dependent pair correlations relative to a third particle in $p+$ Au and $d+$ Au collisions at RHIC, Phys. Lett. B **798**, 134975 (2019).

[15] M. S. Abdallah *et al.* (STAR Collaboration), Pair invariant mass to isolate background in the search for the chiral magnetic effect in Au + Au collisions at $\sqrt{s_{NN}} = 200$ GeV, Phys. Rev. C **106**, 034908 (2022).

[16] M. Abdallah *et al.* (STAR Collaboration), Search for the chiral magnetic effect via charge-dependent azimuthal correlations relative to spectator and participant planes in Au+Au collisions at $\sqrt{s_{NN}} = 200$ GeV, Phys. Rev. Lett. **128**, 092301 (2022).

[17] V. Khachatryan *et al.* (CMS Collaboration), Observation of charge-dependent azimuthal correlations in p-Pb collisions and its implication for the search for the chiral magnetic effect, Phys. Rev. Lett. **118**, 122301 (2017).

[18] A. M. Sirunyan *et al.* (CMS Collaboration), Constraints on the chiral magnetic effect using charge-dependent azimuthal correlations in pPb and PbPb collisions at the CERN Large Hadron Collider, Phys. Rev. C **97**, 044912 (2018).

[19] S. Acharya *et al.* (ALICE Collaboration), Constraining the magnitude of the chiral magnetic effect with event shape engineering in Pb-Pb collisions at $\sqrt{s_{\mathrm{NN}}} = 2.76$ TeV, Phys. Lett. B **777**, 151 (2018).

[20] S. Acharya *et al.* (ALICE Collaboration), Constraining the Chiral Magnetic Effect with charge-dependent azimuthal correlations in Pb-Pb collisions at $\sqrt{s_{\mathrm{NN}}} = 2.76$ and 5.02 TeV, J. High Energy Phys. 09 (2020) 160.

[21] F. Wang, Effects of cluster particle correlations on local parity violation observables, Phys. Rev. C **81**, 064902 (2010).

[22] A. Bzdak, V. Koch, and J. Liao, Remarks on possible local parity violation in heavy ion collisions, Phys. Rev. C **81**, 031901(R) (2010).

[23] S. Schlichting and S. Pratt, Charge conservation at energies available at the BNL Relativistic Heavy Ion Collider and contributions to local parity violation observables, Phys. Rev. C **83**, 014913 (2011).

[24] B. Aboona *et al.* (STAR Collaboration), Search for the Chiral Magnetic Effect in Au+Au collisions at $\sqrt{s_{\mathrm{NN}}} = 27$ GeV with the STAR forward Event Plane Detectors, Phys. Lett. B **839**, 137779 (2023).

[25] M. Abdallah *et al.* (STAR Collaboration), Search for the chiral magnetic effect with isobar collisions at $\sqrt{s_{NN}} = 200$ GeV by the STAR collaboration at the BNL relativistic heavy ion collider, Phys. Rev. C **105**, 014901 (2022).

[26] H.-J. Xu, X. Wang, H. Li, J. Zhao, Z.-W. Lin, C. Shen, and F. Wang, Importance of isobar density distributions on the chiral magnetic effect search, Phys. Rev. Lett. **121**, 022301 (2018).

[27] H. Li, H. J. Xu, J. Zhao, Z. W. Lin, H. Zhang, X. Wang, C. Shen, and F. Wang, Multiphase transport model predictions of isobaric collisions with nuclear structure from density functional theory, Phys. Rev. C **98**, 054907 (2018).

[28] H.-j. Xu, H. Li, X. Wang, C. Shen, and F. Wang, Determine the neutron skin type by relativistic isobaric collisions, Phys. Lett. B **819**, 136453 (2021).

[29] D. E. Kharzeev, J. Liao, and S. Shi, Implications of the isobar-run results for the chiral magnetic effect in heavy-ion collisions, Phys. Rev. C **106**, L051903 (2022).

[30] Y. Feng (STAR Collaboration), Estimate of a nonflow baseline for the chiral magnetic effect in isobar collisions at RHIC, EPJ Web Conf. **276**, 06013 (2023).

[31] M. I. Abdulhamid *et al.* (STAR Collaboration), companion paper, Upper limit on the Chiral Magnetic effect in isobar collisions at the relativistic heavy-ion collider, Phys. Rev. Res. **6**, L032005 (2024).

[32] J. Adams *et al.* (STAR Collaboration), Azimuthal anisotropy in Au+Au collisions at $\sqrt{S_{NN}} = 200$-GeV, Phys. Rev. C **72**, 014904 (2005).

[33] A. Bilandzic, N. van der Kolk, J.-Y. Ollitrault, and R. Snellings, Event-plane flow analysis without non-flow effects, Phys. Rev. C **83**, 014909 (2011).

[34] A. M. Poskanzer and S. A. Voloshin, Methods for analyzing anisotropic flow in relativistic nuclear collisions, Phys. Rev. C **58**, 1671 (1998).

[35] J.-Y. Ollitrault, A. M. Poskanzer, and S. A. Voloshin, Effect of flow fluctuations and nonflow on elliptic flow methods, Phys. Rev. C **80**, 014904 (2009).

[36] D. Shen, J. Chen, A. Tang, and G. Wang, Impact of globally spin-aligned vector mesons on the search for the chiral magnetic effect in heavy-ion collisions, Phys. Lett. B **839**, 137777 (2023).

[37] H. Wieman *et al.* (STAR Collaboration), STAR TPC at RHIC, IEEE Trans. Nucl. Sci. **44**, 671 (1997).

[38] M. Anderson *et al.*, The Star time projection chamber: A Unique tool for studying high multiplicity events at RHIC, Nucl. Instrum. Meth. Phys. Res. A **499**, 659 (2003).

[39] W. Llope, F. Geurts, J. Mitchell, Z. Liu, N. Adams *et al.*, The TOFp / pVPD time-of-flight system for STAR, Nucl. Instrum. Methods Phys. Res., Sect. A **522**, 252 (2004).

[40] C. Adler *et al.*, The RHIC zero-degree calorimeters, Nucl. Instrum. Meth. Phys. Res. A **499**, 433 (2003).

[41] B. I. Abelev *et al.* (STAR Collaboration), Systematic measurements of identified particle spectra in pp, d^{+} Au and Au+Au collisions from star, Phys. Rev. C **79**, 034909 (2009).

[42] J. Adams *et al.* (STAR Collaboration), Delta phi delta eta correlations in central Au+Au collisions at s(NN)**(1/2) = 200-Gev, Phys. Rev. C **75**, 034901 (2007).

[43] G. Agakishiev *et al.* (STAR Collaboration), Anomalous centrality evolution of two-particle angular correlations from Au-Au collisions at $\sqrt{s_{\mathrm{NN}}} = 62$ and 200 GeV, Phys. Rev. C **86**, 064902 (2012).

[44] S. Acharya *et al.* (ALICE Collaboration), Two particle differential transverse momentum and number density correlations in p-Pb and Pb-Pb at the LHC, Phys. Rev. C **100**, 044903 (2019).

[45] A. Aduszkiewicz *et al.* (NA61/SHINE), Two-particle correlations in azimuthal angle and pseudorapidity in central ^{7}Be + ^{9}Be collisions at the CERN super proton synchrotron, Eur. Phys. J. C **80**, 1151 (2020).

[46] L. Adamczyk *et al.* (STAR Collaboration), Long-range pseudorapidity dihadron correlations in $d+$ Au collisions at $\sqrt{s_{\mathrm{NN}}} = 200$ GeV, Phys. Lett. B **747**, 265 (2015).

[47] The STAR Collaboration, Measurement of flow coefficients in high-multiplicity p+Au, d+Au and ^{3}He+Au collisions at $\sqrt{s_{\mathrm{NN}}} = 200$ GeV, arXiv:2312.07464 [nucl-ex].

[48] S. Chatrchyan *et al.* (CMS Collaboration), Multiplicity and transverse momentum dependence of two- and four-particle correlations in pPb and PbPb collisions, Phys. Lett. B **724**, 213 (2013).

[49] G. Aad *et al.* (ATLAS Collaboration), Measurement of long-range pseudorapidity correlations and azimuthal harmonics in $\sqrt{s_{NN}} = 5.02$ TeV proton-lead collisions with the ATLAS detector, Phys. Rev. C **90**, 044906 (2014).

[50] N. M. Abdelwahab *et al.* (STAR Collaboration), Isolation of flow and nonflow correlations by two- and four-particle cumulant measurements of azimuthal harmonics in $\sqrt{s_{NN}} = 200$ GeV Au+Au collisions, Phys. Lett. B **745**, 40 (2015).

[51] J. Adam *et al.* (ALICE Collaboration), Anisotropic flow of charged particles in Pb-Pb collisions at $\sqrt{s_{\mathrm{NN}}} = 5.02$ TeV, Phys. Rev. Lett. **116**, 132302 (2016).

[52] C. Aidala *et al.* (PHENIX Collaboration), Creation of quark-gluon plasma droplets with three distinct geometries, Nature Phys. **15**, 214 (2019).

[53] U. A. Acharya *et al.* (PHENIX Collaboration), Kinematic dependence of azimuthal anisotropies in $p+Au, d+Au$, and $^{3}He+Au$ at $\sqrt{s_{NN}} = 200$ GeV, Phys. Rev. C **105**, 024901 (2022).

[54] J. L. Nagle, R. Belmont, S. H. Lim, and B. Seidlitz, Checking nonflow assumptions and results via PHENIX published cor-

relations in $p+p$, $p+$Au, $d+$Au, and ^{3}He +Au at $\sqrt{s_{NN}}=$ 200 GeV, Phys. Rev. C **105**, 024906 (2022).

[55] J. Adams *et al.* (STAR Collaboration), Azimuthal anisotropy and correlations at large transverse momenta in p+p and Au+Au collisions at s(NN)**(1/2) = 200-GeV, Phys. Rev. Lett. **93**, 252301 (2004).

[56] G. Yan, Probing Initial- and Final-state Effects of Heavy-ion Collisions with STAR Experiment, Proceedings, 29th International Conference on Ultrarelativistic Nucleus-Nucleus Collisions (Quark Matter 2022): Krakow, Poland, April 4–10, 2022, Acta Phys. Pol. B Proc. Suppl. **16**, 1-A137 (2023).

[57] H. Li, H. J. Xu, Y. Zhou, X. Wang, J. Zhao, L. W. Chen, and F. Wang, Probing the neutron skin with ultrarelativistic isobaric collisions, Phys. Rev. Lett. **125**, 222301 (2020).

[58] H. J. Xu, W. Zhao, H. Li, Y. Zhou, L. W. Chen, and F. Wang, Probing nuclear structure with mean transverse momentum in relativistic isobar collisions, Phys. Rev. C **108**, L011902 (2023).

[59] G. Giacalone, Observing the deformation of nuclei with relativistic nuclear collisions, Phys. Rev. Lett. **124**, 202301 (2020).

[60] G. Giacalone, J. Jia, and V. Somà, Accessing the shape of atomic nuclei with relativistic collisions of isobars, Phys. Rev. C **104**, L041903 (2021).

[61] C. Zhang and J. Jia, Evidence of Quadrupole and Octupole Deformations in Zr96+Zr96 and Ru96+Ru96 Collisions at Ultrarelativistic Energies, Phys. Rev. Lett. **128**, 022301 (2022).

[62] S. Bhatta, C. Zhang, and J. Jia, Energy dependence of heavy-ion initial condition in isobar collisions, arXiv:2301.01294 [nucl-th].

[63] X.-N. Wang and M. Gyulassy, HIJING: A Monte Carlo model for multiple jet production in p p, p A and A A collisions, Phys. Rev. D **44**, 3501 (1991).

[64] M. Gyulassy and X.-N. Wang, HIJING 1.0: A Monte Carlo program for parton and particle production in high-energy hadronic and nuclear collisions, Comput. Phys. Commun. **83**, 307 (1994).

[65] Y. Feng, J. Zhao, H. Li, H. J. Xu, and F. Wang, Two- and three-particle nonflow contributions to the chiral magnetic effect measurement by spectator and participant planes in relativistic heavy ion collisions, Phys. Rev. C **105**, 024913 (2022).

[66] Y. Feng, Y. Lin, J. Zhao, and F. Wang, Revisit the chiral magnetic effect expectation in isobaric collisions at the relativistic heavy ion collider, Phys. Lett. B **820**, 136549 (2021).

[67] S. A. Voloshin, Testing the chiral magnetic effect with central U+U collisions, Phys. Rev. Lett. **105**, 172301 (2010).

[68] W.-T. Deng, X.-G. Huang, G.-L. Ma, and G. Wang, Test the chiral magnetic effect with isobaric collisions, Phys. Rev. C **94**, 041901(R) (2016).

[69] G. J. Feldman and R. D. Cousins, A Unified approach to the classical statistical analysis of small signals, Phys. Rev. D **57**, 3873 (1998).

[70] The STAR Beam Use Request for Run-23-25, https://drupal.star.bnl.gov/STAR/files/STAR_BUR_Runs23_25_2022.pdf.

[71] STAR BUR Runs 24-25, https://indico.bnl.gov/event/20331/attachments/49219/83916/STAR_BUR_Runs24_25_2023.pdf (2023).